

Porosity and Permeability Prediction through Forward Stratigraphic Simulations Using GPM™ and Petrel™: Application in Shallow Marine Depositional Settings.

Daniel Otoo and David Hodgetts

Department of Earth and Environmental Sciences, University of Manchester, Manchester, M13 9PL, United Kingdom.

Correspondence to: Daniel Otoo (daniel.otoo@manchester.ac.uk)

Abstract

The forward stratigraphic simulation approach is applied to predict porosity and permeability distribution. Synthetic well logs from the forward stratigraphic model served as secondary data to control porosity and permeability representation in the reservoir model. Building a reservoir model that fits data at different locations comes with high levels of uncertainty. Therefore, it is critical to generate an appropriate stratigraphic framework to guide lithofacies and associated porosity/permeability simulation. The workflow adopted for this task is in three parts; first, simulation of twenty scenarios of sediment transportation and deposition using the geological process modeling (GPM™) software developed by Schlumberger. Secondly, an estimation of the extent and proportion of lithofacies units in the stratigraphic model using the property calculator tool in Petrel™. Finally, porosity and permeability values are assigned to corresponding lithofacies-units in the forward stratigraphic model to produce a forward stratigraphic-based porosity and permeability model. Results show a forward stratigraphic-based lithofacies model, which depends on sediment diffusion rate, sea level variation, sediment movement, wave processes, and tectonic events. This observation is consistent with the natural occurrence, where variation in sea level, sediment supply, and accommodation control stratigraphic sequences, and therefore, facies distribution in a geological basin. Validation wells VP1 and VP2 showed a notable match after a comparing the original and forward stratigraphic-based porosity models. However, a significant discrepancy is recorded in the permeability estimates. These results suggest that the forward stratigraphic modeling approach can be a practical addition to geostatistical-based workflows for realistic prediction of porosity and permeability.

1 **Introduction**

2 The distribution of reservoir properties such as porosity and permeability is a direct function of a complex
3 combination of sedimentary, geochemical, and mechanical processes (Skalinski & Kenter, 2014). The
4 impact of reservoir petrophysics on well planning and production strategies makes it imperative to use
5 reservoir modeling techniques that present realistic property variations via 3-D models (Deutsch and
6 Journel, 1999; Caers and Zhang, 2004; Hu & Chugunova, 2008). Typically, reservoir modeling requires
7 continued property modification until an appropriate match to subsurface data. Meanwhile, subsurface
8 data acquisition is expensive, thus restricts data collection and accurate subsurface property modeling.
9 Several studies, Hodgetts et al. (2004) and Orellana et al. (2014) have demonstrated how stratigraphic
10 patterns, and therefore petrophysical attributes in seismic data, outcrops, and well logs are applicable in
11 subsurface modeling. However, the absence of detailed 3-dimensional depositional frameworks to guide
12 property modeling inhibits the use of stratigraphic patterns to capture subsurface property variations
13 (Burgess et al. 2008). Reservoir modeling techniques with the capacity to integrate forward stratigraphic
14 simulation outputs with stochastic modeling techniques for subsurface property modeling will improve
15 reservoir heterogeneity characterization, because they more accurately produce geological realism than
16 the other modeling methods (Singh et al. 2013). The use of geostatistical-based methods to represent
17 spatial variability of reservoir properties has been in many exploration and production projects (Kelkar
18 and Godofredo, 2002). In the geostatistical modeling method, an alternate numerical 3-D model
19 (realizations) shows different property distribution scenarios that are most likely to match well data
20 (Ringrose & Bentley, 2015). However, due to cost, reservoir modeling practitioners continue to encounter
21 the challenge of obtaining adequate subsurface data to deduce reliable variograms for geostatistical-based
22 subsurface modeling, therefore introducing a significant level of uncertainty in reservoir models (Orellana
23 et al. 2014). The advantages of applying geostatistical modeling approaches to represent subsurface
24 properties in models are discussed in studies by Deutsch and Journel (1999), Dubrule, (1998). A notable
25 disadvantage is that the geostatistical modeling method tends to confine reservoir property distribution to
26 subsurface data and rarely produces geological realism to capture sedimentary events that led to reservoir

27 formation (Hassanpour et al. 2013). In effect, the geostatistical modeling technique does not reproduce
28 long-range continuous reservoir properties, which are essential for generating realistic reservoir
29 connectivity models (Strebelle & Levy, 2008). In their work, Christ et al. (2016) illustrate the use of
30 forward stratigraphic modeling for reconstructing subsurface patterns. The forward stratigraphic
31 modeling method operates on the guiding principle that multiple sedimentary process simulations in a
32 3-D framework will provide geologic details to improve the modeling of stratigraphic sequences, and
33 therefore facies and petrophysical property distribution in an existing basin model. Given this, the forward
34 stratigraphic simulation approach was applied in this contribution to forecast lithofacies, porosity, and
35 permeability in a reservoir model. A significant aspect of this work is using variogram parameters from
36 forward stratigraphic-based synthetic wells to simulate porosity and permeability trends in the reservoir
37 model.

38 The geological process modeling GPM™ software (Schlumberger, 2017) is used to replicate sediment
39 depositional processes in the model area to realize realistic stratigraphic sequences for porosity and
40 permeability prediction. The reservoir interval under study is within the Hugin formation. Studies by
41 Varadi et al. (1998); Kieft et al. (2011) indicate that the Hugin formation was formed through a complex
42 depositional architecture of waves, tidal, and fluvial processes. This knowledge suggests that a single
43 depositional model will not be adequate to produce a realistic lithofacies or petrophysical distributions
44 model of the area. Furthermore, the indication of a complicated Syn-depositional rift-related faulting
45 system by Milner and Olsen, 1998, significantly influences the stratigraphic architecture of the model
46 area. Therefore, the contribution seeks to produce a depositional sequence, which captures subsurface
47 attributes observed in seismic and well data to guide porosity and permeability modeling.

48 **Study Area**

49 The Volve field (Figure 1), located in Block 15/9 south of the Norwegian North Sea, has the Hugin
50 Formation as the reservoir interval from which hydrocarbons are produced (Vollset and Dore, 1984). The
51 Hugin formation, which is Jurassic in age (late Bajocian to Oxfordian), is made up of shallow marine to
52 marginal marine sandstone deposits, coals, and a significant influence of wave events that tend to control

53 lithofacies distribution in the formation (Varadi et al. 1998; and Kieft et al. 2011). Studies by Sneider et
54 al. (1995) and Husmo et al. (2003) associate sediment deposition into the study area to rift-related
55 subsidence and successive flooding during a large transgression of the Viking Graben within the Middle
56 to Late Jurassic period. Also, Cockings et al. (1992), Milner and Olsen (1998) indicate that the Hugin
57 formation comprises of marine shoreface, lagoonal and associated coastal plain, back-stepping delta-
58 plain, and delta front. However, recent studies by Folkestad and Satur (2006) also provide evidence of a
59 high tidal event, which introduces another dimension that requires attention in any subsurface modeling
60 task in the study area. The thickness of the Hugin formation is estimated between 5 m and 200 m, but can
61 be thicker off-structure and non-existent on structurally high segments due to post-depositional erosion
62 (Folkestad and Satur, 2006).

63 A summarised sedimentological delineation within the Hugin formation is presented based on studies by
64 Kieft et al. (2011). In **Table 1**, lithofacies-association codes A, B, C, D, and E represent bay fill units,
65 shoreface sandstone facies, mouth bar units, fluvio-tidal channel fill sediments, and coastal plain facies
66 units, respectively. Additionally, a lithofacies association prefixed code F, which consists of open marine
67 shale units, mudstone. Within it are occasional siltstone beds, parallel laminated soft sediment
68 deformation that locally develop at bed tops. The lateral extent of the code F lithofacies package in the
69 Hugin formation is estimated to be 1.7 km to 37.6 km, but the total thickness of code F lithofacies is not
70 known (Folkestad & Satur, 2006).

71 **Data and Software**

72 This work is based on the description and interpretation of petrophysical datasets in the Volve field by
73 Equinor. Datasets include 3-D seismic and a suite of 24 wells that consist of formation pressure data, core
74 data, petrophysical and sedimentological logs. Previous studies by Folkestad & Satur (2006) and Kieft et
75 al., (2011) in this reservoir interval show varying grain size, sorting, sedimentary structures, bounding
76 contacts of sediment matrix. Grain size, sediment matrix, and the degree of sorting will typically drive
77 the volume of the void created, and therefore the porosity and permeability attributes. Wireline-log
78 attributes such as gamma-ray (GR), sonic (DT), density (RHOB), and neutron-porosity (NPHI)

79 distinguish lithofacies units, stratigraphic horizons, and zones that are essential for building the 3-D
80 property model in Schlumberger's Petrel™ software. Besides, this study also seeks to produce a realistic
81 depositional model like the natural stratigraphic framework in a shallow marine depositional setting.
82 Therefore, obtaining a 3-dimensional stratigraphic model that shows a similar stratigraphic sequence
83 observed in the seismic data allows us to deduce variogram parameters to serve as input in actual
84 subsurface property modeling.

85 Twenty forward stratigraphic simulations were produced in the geological process modeling (GPM™)
86 software to illustrate depositional processes that resulted in the build-up of the reservoir interval under
87 study. By the fourth simulation, there was a development of stratigraphic patterns that shows similar
88 sequences as those observed in seismic, hence the decision to constrain the simulation to twenty scenarios.
89 Delft3D-Flow™ and DIONISOS™ are examples of subsurface process modeling software used in
90 previous studies such as Rijin & Walstra, (2003) and Burges et al. (2008). The availability of the GPM™
91 software license and the capacity to integrate stratigraphic simulation outputs in the property modeling
92 workflow in Petrel™ is the reason for using the geological process modeling software in this study.

93 **Methodology**

94 The workflow (Figure 2a) combines the stratigraphic simulation capacity of GPM™ in different
95 sedimentary processes and the property modeling tools in Petrel™ to predict the distribution of porosity
96 and permeability properties away from known data. This involves three broad steps: (i) forward
97 stratigraphic simulation in GPM™ (2019.1 version), (ii) lithofacies classification using the calculator tool
98 in Petrel™, and (iii) porosity and permeability modeling in Petrel™ (2019.1 version).

99 **Forward Stratigraphic Simulation in GPM™**

100 GPM™ is commercial software developed by Schlumberger to simulate clastic and carbonate
101 sedimentation in a deep or shallow marine environment. GPM™ consists of geological processes such as
102 steady flow, sediment diffusion, tectonics, and sediment accumulation that rely on physical equations and
103 assumptions to replicate the process of sedimentation in a geological basin. A realistic realization of a

104 stratigraphic pattern as observed in seismic or well data provides a 3-dimensional framework to constrain
105 subsurface property representation that conforms with the real-world property distribution trends. In
106 clastic sedimentation, the movement of sediments relies on equations from the original SEDSIM
107 developed in Stanford University (Harbaugh, 1993). Sediment movement, erosion, and deposition is
108 governed by a simplified Navier Stokes equation. “Simplified” because the Navier-Stokes equation in its
109 original form define sediment movement in a 3-dimensions differential form, while the flow equation in
110 GPMTM is 2-dimensional with an arbitrary input of flow depth. Kieft et al. (2011) describe the influence
111 of a combination of fluvial and wave processes in the genetic structure of sediments in the Hugin
112 formation. These geological processes are rapid, depending on accommodation generated by sea-level
113 variation and or sediment composition and flow intensity. The deposition of sediments into a geological
114 basin and its response to post-depositional sedimentary or tectonic processes are significant in the ultimate
115 distribution of subsurface lithofacies and petrophysics. Therefore, several input parameters for the
116 forward simulation to attain a stratigraphic output that fits existing knowledge of paleo-sediment
117 transportation and deposition into the study area (see Table 2). The forward simulation at all stages
118 portrayed geological realism concerning stratigraphic sequence, but it also revealed some limitations,
119 such as instability in the simulator when more than three geological processes run concurrently. Given
120 this, the diffusion and tectonic processes remained constant whiles varying the steady flow, unsteady
121 flow, and sediment accumulation processes in each simulation run.

122 **Steady & Unsteady Flow Process**

123 The steady flow process in GPM simulates flows that change slowly over a period, or sediment transport
124 scenarios where flow velocity and channel depth do not vary abruptly e.g. rivers at a normal stage, deltas,
125 and sea currents. Considering the influence of fluvial activities during sedimentation in the Hugin
126 formation, it is significant to capture its impact on the resultant simulated output.

127 The unsteady flow process can simulate periodic flows such as turbidites where the occurrence is not
128 regular, and the velocity of flow changes abruptly over time. The unsteady flow process applies several
129 fluid elements driven by gravity and friction against the hypothetical topographic surface. Otoo and

130 Hodgetts (2019) illustrate how the unsteady process in GPMTM attains realistic distribution of lithofacies
 131 units in a turbidite fan system. Although the steady and unsteady flow governing equations distantly rely
 132 on the Navier-Stokes equations, the steady flow is quite distinct, as it uses a finite difference numerical
 133 method for faster computation and to also illustrate the frequency of flow that is characteristic in channel
 134 flow such as rivers. The finite difference method applies an assumption that flow velocity is constant
 135 from channel bottom to surface. In contrast, the unsteady flow uses the particle method from SEDSIM3
 136 to solve the sediment concentration in flow and sediment transport capacity (Tetzlaff & Harbaugh 1989).
 137 The simplified equation in GPMTM attempts to solve the problem of “shallow-water free-surface flow”
 138 over an arbitrary topography surface (Tetzlaff, D. personal communication, February 2021). “Shallow
 139 water” indicates the instance where only the vertically-averaged flow velocity and flow depth are applied
 140 and kept track of as a function of two horizontal coordinates.

141 The equation that control steady and unsteady flow is expressed through:

$$142 \quad \frac{\partial h}{\partial t} + \nabla \cdot hQ = 0 \quad (1)$$

143 Where: h is flow depth, t is time, and Q the horizontal flow velocity vector.

$$144 \quad \left(\frac{\partial Q}{\partial t}\right) = -(g\nabla)H + \frac{c_2}{\rho} \nabla^2 Q - \frac{c_2 Q/Q}{h} \quad (2)$$

145 Where: $\frac{\partial Q}{\partial t}$ is the Lagrangian derivative of flow relative to time, g is gravity, H is the water surface
 146 elevation, c_2 is the fluid friction coefficient, ρ is the water density, c_1 is the water friction coefficient and
 147 h is the flow depth.

148 The Manning’s equation is applied to relate flow, slope, flow depth and hydraulic radius channels with a
 149 constant cross-section for the steady flow process. Manning’s formula states:

$$150 \quad V = \frac{k}{n} R_h^{2/3} S^{1/2} \quad (3)$$

151 Where: V is the flow velocity, k is the unit conversion factor, n is the Manning’s coefficient which
 152 depends on channel rugosity, R_h is the hydraulic radius and S is the slope.

153 As mentioned earlier, the unsteady flow process uses the particle method equation, which relies on the
 154 assumption that erosion and deposition depend on the balance between the flow's transport capacity and
 155 the "effective sediment concentration". The equation for multiple-sediment transport in flow is given as
 156 follows:

$$157 \quad A_{em} = \sum_{k_s} \frac{l_{K_s}}{f_{1k_s}} \quad (4)$$

158 Where: A_{em} is the effective sediment concentration of mixture, l_{k_s} is the sediment concentration of each
 159 type, and f_{1,k_s} is the transportability of each sediment type.

160 The transport capacity of a sediment type is expressed by equations (5) and (6). Let consider

$$161 \quad R = (A - A_{em})f_{2,k_s} \quad (5)$$

162 Where f_{2,k_s} is the erosion-deposition rate coefficient for sediment type k_s . For every sediment type k_s ,
 163 the formula for transporting sediment of different grain sizes is given as:

$$164 \quad (H - Z) \frac{Dl_{K_s}}{Dt} = \begin{cases} R & \text{if } R > 0 \text{ and } \tau_0 \geq f_{3,k_s} \text{ and } k(x, y, z) = K_s \\ & \text{or } R < 0 \text{ and } K_s = 1 \text{ or } l_{k_s-1} = 0 \\ 0 & \text{otherwise} \end{cases} \quad (6)$$

165 Where;

166 H is the free surface elevation to sea level, Z is the topographic elevation for sea level, K_s is the sediment
 167 type, l_{k_s} is the volumetric sediment concentration of a specific type (k).

168 **Sediment Diffusion Process**

169 The diffusion process replicates sediment movement from a higher slope (source location) and deposition
 170 into a lower elevation of the model area. Sediment diffusion runs on the assumption that sediments are
 171 transported downslope at a proportional rate to the topographic gradient, making fine-grained sediments
 172 easily transportable than coarse-grained sediments. Sediment diffusion depends on three parameters: (i)
 173 sediment grain size and turbulence in the flow, (ii) diffusion curve that serves as a unitless multiplier in
 174 the algorithm and, (iii) diffusion coefficient. The diffusion coefficient depends, among other variables on

175 the type of sediment and “energy” of the depositional environment. In this contribution, the highest depth-
 176 dependent diffusion coefficient occurs near sea level, where the “energy” is highest over a geological
 177 time (Dashtgard et al. 2007).

178 In GPMTM, sediment diffusion is calculated using a simplified expression:

$$179 \quad \frac{\partial z}{\partial t} = D_i \nabla^2 z + S_n \quad (7)$$

180 where z is topographic elevation, D_i is the diffusion coefficient, t for time, and $\nabla^2 z$ is the laplacian of z ,
 181 and S_n is the sediment source term.

182 Sediment diffusion (D_i) is estimated by assuming that the grain size for each sediment component (coarse
 183 sand, fine sand, silt, and clay) are known. Also an assumption that these sediment types have a uniform
 184 diameter (D) in the flow mix (Dade & Friend 1998; and Zhong 2011). In that case, external fore (F_e),
 185 which consist of drag, lift, virtual mass, and Basset history force is given as:

$$186 \quad F_e = \alpha_e M_e + \alpha_e \Phi_D \frac{U_{fi} - U_{ei}}{T_p} \quad (8)$$

187 M_e is the resultant force of other forces with the exception of drag force, T_p stokes relation time, expressed
 188 as: $T_p = \rho_p D^2 / (18 \rho_f \nu_f)$, with ρ_f and ν_f as density and viscosity of fluid respectively. Φ_D is a coefficient
 189 that accounts for the non-linear dependence of drag force on grain slip Reynolds number (R_p).

$$190 \quad \Phi_D = \frac{R_p}{24} C_D \quad (9), \text{ with } C_D \text{ sediment grain coefficient.}$$

191 With the flow component in place, the diffusion coefficient (D_i) is deduced from the Einstein equation.
 192 Using an assumption that the diffusion coefficient decreases with increasing grain size and rise in
 193 temperature, and that the coefficient f is known, the expression for D_i is:

$$194 \quad D_i = \frac{K_B \cdot T}{f} \quad (10)$$

195 Meanwhile, f is a function of the dimension of the spherical particle involved at a particular time (t). In
 196 accounting for f , the equation for D_i changes into:

197
$$D_i = \frac{K_B.T}{6.\pi.\eta_o.r} \quad (11)$$

198 **Sediment Accumulation**

199 The sediment accumulation process in GPM is designed to generate an arbitrary amount of sediment
 200 representing the artificial vertical thickness of a lithology as interpreted in a well or outcrop data (Tetzlaff,
 201 D., personal communication, February 2021). The areal input rates for each sediment type (coarse-
 202 grained, fine-grained sediments) use the value of the map surface at each cell in the model and multiply
 203 it by a value from a unitless curve at each time step in the simulation to estimate the thickness of sediments
 204 accumulated or eroded from a cell in the model. Sediment accumulation in the GPM software requires
 205 other processes such as steady flow and diffusion to account for sediment transport (sediment entering or
 206 leaving a cell) before a deposition/year (mm/yr) function to artificially produce the height of sediment
 207 deposited per cell. The accumulation of sediments in GPM is expressed as:

208
$$A_T = \sum_{S=1}^n [(M_{v1} * S_{c1}), \dots n] \quad (12)$$

209 Where;

210 A_T is the total sediment accumulated in a cell over a period, S is the sediment type, M_v is the map value
 211 of sediment in each cell, and S_C is the sediment supply curve as a function of topographic elevation.

212 **Boundary Conditions for Forward Stratigraphic Simulation**

213 Realistic reproduction of stratigraphic patterns in the model area requires input parameters (initial
 214 conditions), such as paleo-topography, sea-level curves, sediment source location, and distribution curve,
 215 tectonic event maps (subsidence and uplift), and sediment mix velocity. The application of these input
 216 parameters in GPMTM and their impact on the resultant stratigraphic framework is below.

217 **Hypothetical Paleo-Surface:** The hypothetical paleo-topographic for the stratigraphic simulation is from the
 218 seismic data (Figure 3), using the assumption that the present day stratigraphic surface (paleo shoreline in Figure
 219 4a) occurred as a result of basin filling over geological time. Since the surface obtained from the seismic section
 220 have undergone various phases of subsidence and uplifts, it is significant to note that the paleo topographic surface
 221 used in this work does not represent an accurate description of the basin at the period of sediment deposition; thus

222 presenting another level of uncertainty in the simulation. To derive an appropriate paleo-topographic for this
223 task, five paleo topographic surfaces (TPr) were generated, by adding or subtracting elevations from the
224 inferred paleo topographic surface (see Figure 4g) using the equation:

$$225 \quad \text{TPr} = \text{Sbs} + \text{EM} \quad (13)$$

226 where, Sbs is the base surface scenario (in this instance, scenario 6), and EM an elevation below and
227 above the base surface.

228 The paleo-topographic surface in scenario 3 (figure 4d) is selected because it produced a stratigraphic
229 sequences that fit the depositional patterns interpreted from the seismic section (Figure 5d).

230 **Sediment Source Location:** Based on regional well correlations in Kieft et al. 2011, and seismic
231 interpretation of the basin structure, the sediment entry point is placed in the north-eastern section of the
232 hypothetical paleo-topography surface. The exact sediment entry point into this basin is unknown, so
233 three entry points were placed at a 4 km radius around the primary location (Figure 3c) to capture possible
234 sediment source locations in the model area. The source position is a positive integer (values greater than
235 zero) to enable sediment movement to other parts of the topographic surface.

236 **Sea Level:** The sea-level curve is deduced from published studies and facies description in shallow marine
237 depositional environments (e.g. Winterer and Bosellini, 1981). To sea level was constrained 30 m for
238 short simulation runs (5000 to 20000 years), but varied with the increasing duration of the simulation (see
239 Table 2). The peak sea-level in the simulation depicts the maximum flooding surface (Figure 5d), and
240 therefore the inferred sequence boundary in the geological process model.

241 **Diffusion and Tectonic Event Rates:** The sediment mix proportion, diffusion rate, and tectonic event
242 functions are from studies such as Walter, (1978), Winterer and Bosellini, (1981), and Burges et al.,
243 (2008). The diffusion and tectonic event rates were increased or reduced to produce a stratigraphic model
244 that fit our knowledge of basin evolution in the study area. For example, in scenario 1 (Figure 6a), the
245 early stages of clinoform development show resemblance to interpreted trends in the seismic section
246 (**Figure 3b**). The process commenced with a diffusion coefficient of 8 m²/a, but it varied at each scenario
247 to obtain diffusion coefficients to improve the model. Excluding the initial topography (Figure 4d), input

248 parameters in geological processes such as wave events, steady/unsteady flow, diffusion, and tectonic
249 events used curve functions to provide variations in the simulation.

250 The sensitivity of input parameters in the forward stratigraphic simulation is notable when there is a
251 change of value in sediment diffusion, and tectonic rates or dimension of the hypothetical topography.
252 For example, a change in sediment source position affects the extent and depth of sediments deposition
253 in the simulation. Shifting the source point to the mid-section of the topography (the mid-point of the
254 topography in a basin-ward direction) resulted in the accumulation of distal elements identical to turbidite
255 lobe systems. This output is consistent with morphodynamic experiments by de Leeuw et al. (2016),
256 where sediment discharge from the basin slope leads to the build-up of basin floor fan units.

257 **Property Classification in Stratigraphic Model**

258 In our opinion, the most appropriate output is the stratigraphic model in **Figure 5d**. This point of view is
259 because, compared to the depositional description in studies such as Folkestad and Satur (2006); Kieft et
260 al. (2011), and the seismic interpretation presents a similar stratigraphic sequence. Sediment distribution
261 in each time step of the simulation was stacked into a single zone framework to attain a simplified model.
262 This strategy assumes that sedimentary processes that lead to the final build-up of genetic related units
263 within zones of the model will not vary significantly over the simulation period. The stratigraphic model
264 (**Figure 5d**) was converted into a 3-D format (20 m x 20 m x 2 m grid cells) for the property modeling in
265 Petrel™.

266 Facies, porosity, and permeability representation in the stratigraphic model was done via a rule based
267 approach in Petrel™ (see **Table 3**). The classification is driven by depositional depth, geologic flow
268 velocity, and sediment distribution patterns as indicated in **Figure 7**. Lithofacies representation in the
269 stratigraphic model relied on the sediment grain size pattern and proximity to sediment source. For
270 example, shoreface lithofacies units are medium-to-coarse grained sediments, which accumulate at a
271 proximal distance to the sediment source. In contrast, mudstone units are confined to fine-grained
272 sediments in the distal section of the simulation domain.

273 Using knowledge from published studies by Kieft et al. (2011) and wireline-log attributes such as gamma
 274 ray, neutron, sonic, and density logs, porosity and permeability variations in the stratigraphic model are
 275 estimated (Table 1). In previous studies on the Sleipner Øst, and Volve field (Equinor, 2006; Kieft et al.
 276 2011), shoreface deposits make up the best reservoir units, while lagoonal deposits formed the worst
 277 reservoir units. With this guide, shoreface sandstone units and mudstone/shale units in the forward
 278 stratigraphic model are best and worst reservoir units respectively. The porosity and permeability values
 279 in Table 4 are from equations in Statoil’s petrophysical report of the Volve field (Equinor, 2016):

$$280 \quad \varnothing_{er} = \varnothing_D + \alpha \cdot (NPHI - \varnothing_D) + \beta \quad (14)$$

281 where \varnothing_{er} is the estimated porosity range, \varnothing_D is density porosity, α and β are regression constants; ranging
 282 between -0.02 – 0.01 and 0.28 – 0.4 respectively, $NPHI$ is neutron porosity. In instances where $NPHI$
 283 values for lithofacies units is not available from the published references, an average of 0.25 was used.

$$284 \quad KLOGH_{er} = 10^{(2 + 8 * PHIF - 5 * VSH)} \quad (15)$$

285 where $KLOGH_{er}$ is the estimated permeability range, VSH is the volume of clay/shale in the lithofacies
 286 unit, and $PHIF$, the fractured porosity. The VSH range between 0.01 – 0.12 for the shoreface units, and
 287 0.78 – 0.88 for lagoonal deposits.

288 **Property Modeling in Petrel™**

289 The workflow (**Figure 2b**) used for subsurface property modeling in Petrel™ is applied to represent
 290 lithofacies, porosity, and permeability properties in the stratigraphic model. These processes involve:

291 (1) Structure modeling: identified faults within the study area are modeled together with interpreted
 292 surfaces from seismic and well correlation to generate the main structural framework, within
 293 which the property model is built. Here, fault pillars and connecting fault bodies are linked to
 294 obtain the kind of fault framework interpreted from the seismic data.

295 (2) Pillar gridding: building a “grid skeleton” made up of a top, middle and base architectures.
 296 Typically, pillars join corresponding corners of every grid cell of the adjacent grid to form the

297 foundation for each cell within the model. The prominent orientation of faults (I-direction) within
298 the model area was in an N-S and NE-SW direction, so the “I-direction” was set to NNE-SSW to
299 capture the general structural description of the area.

300 (3) Horizons, Zones, and Vertical Layering: stratigraphic horizons and subdivisions (zones) delineate
301 the geological formation’s boundaries. As stratigraphic horizons are introduced into the model
302 grid, the surfaces are trimmed iteratively and modified along faults to correspond with
303 displacements across multiple faults. Vertical layering shows the thicknesses and orientation
304 between the layers of the model. Layers refers to significant changes in particle size or sediment
305 composition in a geological formation. Using a vertical layering scheme makes it possible to honor
306 the fault framework, pillar grid, and horizons. A constant cell thickness of 1 m is used in the model
307 to control the vertical scale of lithofacies, porosity, and permeability modeling.

308 (4) Upscaling: involves the substitution of smaller grid cells with coarser grid cells. Here, log data is
309 transformed from 1-dimensional to a 3-dimensional framework to evaluate which discrete value
310 suits selected data point in the model. One advantage of the upscaling procedure is to make the
311 modeling process faster.

312 **Porosity and Permeability Modeling**

313 The Volve field petrophysical model from Equinor is the base (reference) model in this work. The model,
314 which covers 17.9 km² was generated with the reservoir management software (RMS), developed by Irap
315 and Roxar (EmersonTM). The petrophysical model has a grid dimension of 108 m x 100 m x 63 m and
316 was compressed by 75.27% of cell size from an approximated cell size of 143 m x 133 m x 84 m. To
317 achieve a comparable model resolution as the Volve field porosity and permeability model, the forward
318 stratigraphic output, which had an initial resolution of 90 m x 78 m x 45 m, is upscaled to a grid of 107
319 m x 99 m x 63 m. Variograms being a critical aspect of this work, we submit two options to extrapolate
320 variogram parameters from the forward stratigraphic-based porosity and permeability models. In Option
321 1, the porosity and permeability values were assigned to the synthetic lithofacies wells that correlate with
322 known facies-association in the study area (see **Table 4**).

323 The pseudo wells comprising porosity and permeability are situated in-between well locations to guide
324 porosity and permeability simulation in the model. For option 2, the best-fit forward stratigraphic model
325 changes by assigning porosity and permeability attribute using the general stratigraphic orientation
326 captured in the seismic data (NE-SW; 240°). Porosity and permeability pseudo (synthetic) logs were then
327 extracted from the forward stratigraphic output to build the porosity and permeability models (**Figure 8**).
328 Porosity modeling is through normal distribution, while the permeability models were produced using a
329 log-normal distribution and the corresponding porosity property for collocated co-kriging.

330 Considering that vertical trends in options 1 and 2 will be similar within a sampled interval, option 2
331 presented a viable 3-D representation of property variations in the major and minor directions of the
332 forward stratigraphic model. Ten synthetic wells (SW), ranging between 80 m and 120 m in total depth
333 (TD), are positioned in the forward model to capture the vertical distribution of porosity-permeability at
334 different sections of the forward stratigraphic-based models.

335 The synthetic wells (**Figure 9 c**) with porosity and permeability data were upscaled, and distributed into
336 the original structural model using the sequential Gaussian simulation method. The synthetic wells
337 derived from the stratigraphic model served as an additional control for porosity and permeability
338 modeling in the Volve field. Because the variogram-based modeling approach is efficient in subsurface
339 data conditioning, this idea presents an opportunity to get more wells at no additional cost to control
340 porosity and permeability distribution. The variogram model (**Figure 10**) of dominant lithofacies units in
341 the stratigraphic model served as a guide in estimating variogram parameters for porosity and
342 permeability modeling. The variogram has major and minor range of 1400 m and 400 m respectively, and
343 an average sill value of 0.75. Six out of fifty model realizations that show some similarity to the original
344 porosity and permeability model formed the basis of our analysis (**Figure 11**). The selection of six
345 realizations was on a visual and statistical comparison of zones in the original Volve field model and the
346 stratigraphic-based porosity/permeability model. The statistical approach involved summary statistics
347 from the reference model and the stratigraphic-based porosity/permeability model. In contrast, the visual
348 evaluation compared the geological realism of forward stratigraphic-based realizations to the base model.

349 **Results**

350 The stratigraphic model in stage 4 (**Figure 5d iv**) shows the final geometry after 700,000 years of
351 simulation time. The initial stratigraphic simulation produced a progradation sequence with foreset-like
352 features (**Figure 5d i**) and a sequence boundary, which separates the initial simulated output from the
353 next prograding phase (**Figure 5d ii**). An aggradational stacking pattern commences and becomes
354 prominent in stage 3 (**Figure 5d iii**). These aggradational sequences observed in the forward stratigraphic
355 model are consistent with natural events where sediment supply matchup with accommodation due to
356 sea-level rise within a geological period (Muto and Steel, 2000; Neal and Abreu, 2009).

357 Impact of the forward stratigraphic simulation on porosity and permeability representation in the reservoir
358 model is evident by comparing its outcomes to the Volve field porosity and permeability models by using
359 two synthetic well (VP1 and VP2); sampled at a 5 m vertical interval. Taking into account the fact that
360 the Volve field petrophysical model (**Figure 11a**) went through various phases of history matching to
361 obtain a model to improve well planning and production strategies, it is reasonable to assume that porosity
362 and permeability distribution in the petrophysical model will be geologically realistic and less uncertain.
363 This view formed the basis for using the porosity and permeability models developed by Equinor as a
364 reference for comparing outputs in the stratigraphic model. **Table 5a** shows an almost good match in
365 porosity at different intervals in the forward stratigraphic-based models (i.e. R14, R20, R26, R36, R45,
366 and R49). An analysis of the well logs in the model area shows that a large proportion of reservoir porosity
367 is between 0.18 – 0.24. Also, the analysis of the forward stratigraphic-based porosity model is consistent
368 with the porosity range in the Volve field model (see Figure 12).

369 A notable limitation with this approach is the assumption that variogram parameters and stratigraphic
370 inclination within zones remained constant throughout the simulation. The difference in permeability
371 attributes between the original permeability model and the forward stratigraphic-based type is the
372 application of other measured parameters in the original model (**Table 5b**). Typically, a petrophysical
373 model like the Sleipner Øst and Volve field model will factor in other datasets such as special core analysis
374 (SCAL) and level of cementation, which enhances reservoir petrophysics assessment. Bearing in mind

375 that the forward stratigraphic model did not involve some of this additional information from the
376 reservoir, it is practicable to suggest that results obtained in the forward stratigraphic-based porosity and
377 permeability models have adequately conditioned to known subsurface data.

378 **Discussion**

379 Results show the influence of sediment transport rate (or diffusion rate), initial basin topography, and
380 sediment source location on the stratigraphic simulation in in GPMTM. Compared to studies such as Muto
381 & Steel (2000) and Neal & Abreu (2009), we observed that a variation in sea-level controls the volume
382 of sediment that is retained or transported further into the basin, therefore controlling the resultant
383 stratigraphic sequences. In related work, Burges et al. (2008) suggest that a sediment-wedge topset width
384 connects directly to the initial bathymetry, in which the sediment-wedge structure develops, and the
385 correlation between sediment supply and accommodation rate. This opinion is in line with observations
386 in this study, where the initial sediment deposit controls the geometry of subsequent phases of depositions
387 in the hypothetical basin. The uncertainty of initial conditions used in this work led to the generation of
388 multiple forward stratigraphic scenarios to account for the range of bathymetries that may have influenced
389 sediment transportation to form the present-day reservoir units in the Volve field.

390 The simulation produced well-defined sloping depositional surfaces in a stratigraphic architecture
391 (clinoforms) and sequence boundaries that depict patterns seen in the seismic data. In their work, Allen
392 and Posamentier (1993); Ghandour and Haredy (2019) explained the importance of sequence stratigraphy
393 in lithofacies characterization, and therefore petrophysical property distribution in sedimentary systems.
394 Also, sediment deposition into a geological basin in the natural order is controlled by mechanical and
395 geochemical processes that modify petrophysical attributes (Warrlich et al. 2010); therefore, using
396 different geological processes and initial conditions to generate depositional scenarios in 3-dimension
397 provides a framework to analyse property variations in a hydrocarbon reservoir. The approach produces
398 a porosity-permeability model comparable to the original petrophysical model using synthetic porosity
399 and permeability logs from the forward stratigraphic model as input datasets. As mentioned, this work
400 did not include variations in the layering scheme that develops in different zones of the stratigraphic

401 model. Under this circumstance, there is a possibility to overestimate and or underestimate porosity and
402 permeability property in some sampled intervals in the validation wells. Therefore, we suggest that the
403 forward stratigraphic simulation outputs such as the example presented in this contribution serve as
404 additional data to understand sediment distribution patterns and associated vertical and horizontal
405 petrophysical trends in the depositional environment, and not as absolute conditioning data in subsurface
406 property modeling.

407 The assumptions made concerning the type of geological processes and input parameters in the
408 stratigraphic simulation certainly differ from what existed during sediment deposition. So, applying
409 stratigraphic models that fit a basin-scale description to a relatively smaller scale reservoir presents
410 another level of uncertainty in this approach. This opinion agrees with Burges et al., (2008), where they
411 indicate that the diffusion geological process simulation fits the description of large-scale sediment
412 transportation. This view further buttresses the point that integrating forward stratigraphic simulation into
413 a well-scale framework has a high chance of producing outcomes that deviate from the real-world
414 subsurface description. In line with observations in Bertonecello et al. (2013); Aas et al. (2014); and Huang
415 et al. (2015) in relations to limitations in the forward stratigraphic simulation method, it is advisable to
416 use its outputs cautiously in reservoir modeling; as such outputs from forward stratigraphic models could
417 lead to an increase in property representation bias in a model.

418 The correlation between reservoir lithofacies and petrophysics, and its prediction through reservoir
419 models, have been extensively examined in several studies (Falivene et al.,2006; Hu and
420 Chugunova,2008). Meanwhile, the predicted outputs most often do not depict the actual reservoir
421 character due to the absence of a realistic 3-D stratigraphic framework to guide reservoir property
422 representation in geological models. The forward stratigraphic modeling method, notwithstanding its
423 limitations, provides reservoir modeling practitioners an platform to generate subsurface models that
424 reflect the natural variation of reservoir properties.

425 **Conclusion**

426 In this paper, synthetic well data from a forward stratigraphic simulation are combined with well data
427 from the Volve field to predict porosity and permeability distribution. The forward stratigraphic modeling
428 scenarios presented in this work do not prove that forward stratigraphic outputs should be used as absolute
429 input parameters for a real-world reservoir modeling task. Considering the uncertainties highlighted in
430 the choice of initial boundary conditions and geological processes for the stratigraphic simulation, it is
431 notable that the simulation produced a depositional architecture that is geologically realistic and
432 comparable to the stratigraphic correlation suggested in published studies of the study area. The match in
433 porosity obtained by comparing validation wells in the original and stratigraphic-based petrophysical
434 model indicates that it is practical to use variogram parameters and or well data from forward stratigraphic
435 simulations for reservoir property modeling. This work also made two key findings:

- 436 1. For specific stratigraphic simulation in GPMTM and a range of model parameters, sediment
437 transportation and deposition is based on diffusion rate and proximity to sediment source. This
438 opinion agrees with several published works on sequence stratigraphy and or system tracts in
439 shallow marine settings. However, further work with different forward stratigraphic modeling
440 simulators could mitigate some of the challenges faced in this work.
- 441 2. A lithofacies distribution that is consistent with previous studies was produced in the stratigraphic
442 model. This is evident in model scenarios where sediment distribution vertically matches with
443 lithofacies variation in a sampled interval in an actual well log.

444 Geologically feasible stratigraphic patterns generated in the forward stratigraphic model provide an
445 additional layer of confidence in representing facies distribution, and therefore porosity/permeability
446 variations in a subsurface model. Furthermore, the resultant forward stratigraphic-based porosity and
447 permeability model suggests that forward stratigraphic modeling can be integrated into geostatistical
448 modeling workflows to improve subsurface property modeling and well planning.

449 **Data and Code Availability**

450 The dataset for this work is from Equinor (Volve field, Norway), and was made available to the public in
451 2018. The data include 24 suits of well logs, and 3-D reservoir models in Eclipse and RMS formats. The
452 data, models (eclipse and RMS formats), and the rule-based calculation script to generate lithofacies and
453 porosity/permeability proportions are archived on Zenodo as Otoo & Hodgetts, (2020).

454 **GPM™ Software**

455 The (2019.1) version of GPM™ software was used in completing this work after an initial 2018.1 version. Available
456 on: <https://www.software.slb.com/products/gpm>. The software license and code used in the GPM™ cannot be
457 provided, because Schlumberger does not allow the code for its software to be shared in publications.

458 **Model Availability in Petrel™**

459 The work started in Petrel™ software (2017.1), but it was completed with Petrel™ software (2019.1).
460 The software is available on: <https://www.software.slb.com/products/petrel>. The software runs on a
461 Windows PC with the following specifications: Processor; Intel Xeon CPU E5-1620 v3 @3.5GHz 4
462 cores-8 threads, Memory; 64 GB RAM. The computer should be high end, because a lot of processing
463 time is required for the task. The forward stratigraphic models are in Zenodo as Otoo & Hodgetts, (2020).

464 **Author Contribution**

465 Daniel Otoo designed the model workflow, conducted the simulation using the GPM™ software,
466 evaluated the results, and drafted the manuscript. David Hodgetts converted the Volve field data into
467 Petrel compactible format and assisted in the revision of the manuscript.

468 **Acknowledgement**

469 Thanks to Equinor for making available the Volve field dataset. Also, thanks to Schlumberger for
470 providing GPM™ software license. A special thanks to Mostfa Legri and Daniel Tetzlaff (Schlumberger)
471 for their technical support in the use of GPM™. Finally, to the Ghana National Petroleum Corporation
472 (GNPC) for sponsoring this research.

473 **References**

- 474 Aas, T., Basani, R., Howell, J. & Hansen, E.: Forward modeling as a method for predicting the distribution of deep-
475 marine sands: an example from the Peira Cava sub-basin. *The geologic society*, 387(1), 247-269,
476 doi:10.1144/SP387.9, 2014.
- 477 Allen, G. P. and Posamentier, H. W.: Sequence stratigraphy and facies model of an incised valley fill; the Gironde
478 Estuary, France. *Journal of Sedimentary Research*; 63 (3), 378–391, doi:/10.1306/D4267B09-2B26-11D7-
479 8648000102C1865D, 1993.
- 480 Bajpai, V.N., Saha Soy, T.K., Tandon, S.K.: Subsurface sediment accumulation patterns and their relationships
481 with tectonic lineaments in the semi-arid Luni river basin, Rajasthan, Western India. *Journal of Arid Environments*,
482 48(4); 603-621, 2001.
- 483 Bertonecello, A., Sun, T., Li, H., Mariethoz, G., & Caers, J.: Conditioning Surface-Based Geological Models to
484 Well and Thickness Data. *International Association of Mathematical Geoscience*, 45, 873-893, doi:
485 10.1007/s11004-013-9455-4, 2013.
- 486 Burges, P.M., Steel, R.J., & Granjeon, D.: Stratigraphic Forward Modeling of Basin-Margin Clinofold Systems:
487 Implications for Controls on Topset and Shelf Width and Timing of Formation of Shelf-Edge deltas. *Recent*
488 *advances in models of siliciclastic shallow-marine stratigraphy. SEPM (Society for Sedimentary Geology) Special*
489 *Publication*, vol. 90, SEPM (Society for Sedimentary Geology), 35-45, 2008.
- 490 Caers, J., & Zhang, T.: Multiple-point geostatistics: a quantitative vehicle for integrating geologic analogs into
491 multiple reservoir models, in Grammer, G. M., Harris, P. M., and Eberli, G. P., eds., *Integration of outcrop and*
492 *modern analogs in reservoir modeling. Am. Assoc. Petrol. Geol. Memoir*, 384–394, 2004.
- 493 Cheng, F., Garzzone, C., Jolivet, M., Guo, Z., Zhang, D., & Zhang, C.: A New Sediment Accumulation Model of
494 Cenozoic Depositional Ages From the Qaidam Basin, Tibetan Plateau. *Journal of Geophysical Research; Earth*
495 *Surface*. 123, 3101-3121, 2018.
- 496 Christ A., Schenk O., Salomonsen P.: Using Stratigraphic Forward Modeling to Model the Brookian
497 Sequence of the Alaska North Slope. In: Raju N. (eds) *Geostatistical and Geospatial Approaches for*
498 *the Characterization of Natural Resources in the Environment (2016)*.
- 499 Cockings, J.H., Kessler, L.G., Mazza, T.A., & Riley, L.A.: Bathonian to mid-Oxfordian Sequence Stratigraphy of
500 the South Viking Graben, North Sea. *Geological Society, London, Special publications*, 67, 65–105,
501 doi:10.1144/GSL.SP.1992.067.01.04, 1992.
- 502 Dade, W.B. & Friend, P.F.: Grain Size, Sediment Transport Regime, and Channel Slope in Alluvial Rivers. *The*
503 *Journal of Geology*, 106(6), 661-676, 1998.
- 504 Dashtgard, S.E., White, R.O., Butler, K.E., Gingras, M.: Effects of relative sea level change on the depositional
505 character of an embayed beach, Bay of Fundy, Canada. *Marine Geology*, 239(3), 143-161, 2007.

506 Deutsch, C. & Journel, A.: GSLIB. Geostatistical software library and user's guide. Geological magazine, 136(1),
507 83-108, doi:10.2307/1270548, 1999.

508 De Leeuw, J., Eggenhuisen, J.T., & Cartigny, M.J.B.: Morphodynamics of submarine channel inception revealed
509 by new experimental approach. Nature Communication, 7, 10886, 2016.

510 Dubrule, O.: Geostatistics in Petroleum Geology. American Association of Petroleum Geologist, 38, 27-101,
511 doi:10.1306/CE3823, 1998.

512 Falivene, O., Arbues, P., Gardiner, A., & Pickup, G.E.: Best practice stochastic facies modeling from a channel-
513 fill turbidite sandstone analog (the Quarry outcrop, Eocene Ainsa basin, northeast Spain. American Association of
514 Petroleum Geologist, 90(7), 1003-1029, doi:10.1306/02070605112, 2006.

515 Folkestad, A., & Satur, N.: Regressive and transgressive cycles in a rift-basin: Depositional model and sedimentary
516 partitioning of the Middle Jurassic Hugin Formation, Southern Viking Graben, North Sea. Sedimentary Geology.
517 207, 1-21, doi:10.1016/j.sedgeo.2008.03.006, 2008.

518 Ghandour, I.M. and Haredy, R.A.: Facies Analysis and Sequence Stratigraphy of Al-Kharrar Lagoon Coastal
519 Sediments, Rabigh Area, Saudi Arabia: Impact of Sea-Level and Climate Changes on Coastal Evolution. Arabian
520 Journal for Science and Engineering, 44(1), 505-520, 2019.

521 Harbaugh, J.W.: Simulating Sedimentary Basins: An Overview of the SEDSIM Model and its Relevance to
522 Sequence Stratigraphy. Geoinformatics, 4(3), 123-126, 1993.

523 Hassanpour, M., Pyrcz, M. & Deutsch, C.: Improved geostatistical models of inclined heterolithic strata for
524 McMurray formation, Canada. AAPG Bulletin, 97(7), 1209-1224, doi:10.1306/01021312054, 2013.

525 Hodgetts, D.D., Drinkwater, N.D., Hodgson, J., Kavanagh, J., Flint, S.S., Keogh, K.J. and Howell, J.A.: Three-
526 dimensional geological models from outcrop data using digital data collection techniques: an example from the
527 Tanqua Karoo depocenter, South Africa. Geological Society, London, v. 171 (4), 57-75,
528 doi:10.1144/GSL.SP.2004.239.01.05, 2004.

529 Hu, L.Y., and Chugunova, T.: Multiple-point geostatistics for modeling subsurface heterogeneity: A
530 comprehensive review. Water Resource Research, 44 (11), 1-14, doi:10.1029/2008WR006993, 2008.

531 Huang, X., Griffiths, C. & Liu, J.: Recent development in stratigraphic forward modeling and its application in
532 petroleum exploration. Australian journal of Earth science, 62(8), 903-919, doi:10.1080/081200991125389, 2015.

533 Husmo, T. & Hamar, G.P. & Høiland, O. & Johannessen, E.P. & Rømuld, A. & Spencer, A.M. & Titterton,
534 Rosemary.: Lower and Middle Jurassic. In: The Millennium Atlas: Petroleum Geology of the Central and Northern
535 North Sea, 129-155, 2003.

536 Kelkar, M., & Perez, G.: Applied Geostatistics for Reservoir Characterization. Society of Petroleum Engineers.
537 [https://www.academia.edu/36293900/Applied Geostatistics for Reservoir characterization](https://www.academia.edu/36293900/Applied_Geostatistics_for_Reservoir_characterization). Accessed 10
538 September, 2019, 2002.

539 Kieft, R.L., Jackson, C.A.-L., Hampson, G.J., and Larsen, E.: Sedimentology and sequence stratigraphy of the
540 Hugin Formation, Quadrant 15, Norwegian sector, South Viking Graben. *Geology Society, London, Petroleum*
541 *Geology Conference Series*, 7, 157-176, doi:10.1144/0070157, 2011.

542 Milner, P.S., and Olsen, T.: Predicted distribution of the Hugin Formation reservoir interval in the Sleipner Øst
543 field, South Viking Graben; the testing of a three-dimensional sequence stratigraphic model. In: Gradstein, F.M.,
544 Sandvik, K.O., Milton, N.J. (Eds.), *Sequence Stratigraphy; Concepts and Applications. Special Publication, Vol 8.*
545 *Norwegian Petroleum Society*, 337-354, 1998.

546 Muto, T., and Steel, R.J.: The accommodation concept in sequence stratigraphy: Some dimensional problems and
547 possible redefinition. *Geology*, 130(1), 1-10, 2000.

548 Neal, J., and Abreu, V.: Sequence stratigraphy hierarchy and the accommodation succession method. *Geology*,
549 37(9), 779-782, 2009.

550 Otoo, D. 2021: Conversation with Daniel Tetzlaff, 4 February.

551 Otoo, D., and Hodgetts, D.: Geological Process Simulation in 3-D Lithofacies Modeling: Application in a Basin
552 Floor Fan Setting. *Bulletin of Canadian Petroleum Geology*, 67(4), 255-272, 2019.

553 Otoo, D. & Hodgetts, D. Data citation for a forward stratigraphic-based porosity and permeability model developed
554 for the Volve field, Norway. Dataset. Zenodo. <http://doi.org/10.5281/zenodo.3855293>, 2020.

555 Orellana, N. Caverro, J. Yemez, I. Singh, V. and Sotomayor, J.: Influence of variograms in 3D reservoir-modeling
556 outcomes: An example. *The leading edge*, 33(8), 890-902, doi:10.1190/tle33080890.1, 2014.

557 Patruno, S., and Hansen, W.H.: Clinoforms and clinoform systems: Review and dynamic classification scheme for
558 shorelines, subaqueous deltas, shelf edges and continental margins. *Earth-Science Reviews*, 185, 202-233, 2018.

559 Ravasi, M., Vasconcelos, I., Curtis, A. and Kristi, A.: Vector-acoustic reverse time migration of Volve ocean-
560 bottom cable data set without up/down decomposed wavefields. *Geophysics* 80 (4): 137-150,
561 doi:10.1190/geo2014-0554.1, 2015.

562 Ringrose., P. & Bentley., M.: *Reservoir model design: A practioner's guide.* First edition ed. New York: Springer
563 business media B.V. 20-150, 2015.

564 Rijn, L.C., Walstra, D.J.R., Grasmeyer, B., Sutherland, J., Pan, S., & Sierra, J.P.: The predictability of cross-shore
565 bed evolution of sandy beaches at the time scale of storms and seasons using process-based profile models. *Coastal*
566 *engineering*, 47(3), 295-327, doi:10.1016/S0378-3839(02)00120-5, 2003.

567 Schlumberger™ Softwares.: *Geological Process Modeling, Petrel™* version 2019.1, Schlumberger, Norway. URL:
568 <https://www.sdc.oilfield.slb.com/SIS/downloads.aspx>, 2019.

569 Sclater, J.G. & Christie, P.A.F.: Continental stretching: An explanation of the Post-Mid-Cretaceous subsidence of
570 the central North Sea Basin. *Journal of Geophysical Research, Solid Earth*; 85(7), 3711-3739, 1980.

571 Singh, V., & Yemez, I., & Sotomayor de la Serna, J.: Integrated 3D reservoir interpretation and modeling: Lessons
572 learned and proposed solutions. *The Leading Edge*. 32(11), 1340-1353, doi:10.1190/tle32111340.1, 2013.

573 Skalinski, M., & Kenter, J.: Carbonate petrophysical rock typing: Integrating geological attributes and
574 petrophysical properties while linking with dynamic behaviour. Geological Society, London, Special Publications.
575 406 (1), 229-259, 2014.

576 Sneider, J.S., de Clarens, P., and Vail, P.R.: Sequence stratigraphy of the Middle and Upper Jurassic, Viking
577 Graben, North Sea. In: Steel, R.J., Felt, V.L., Johannessen, E.P., Mathieu, C. (Eds.), *Sequence Stratigraphy on the*
578 *Northwest European Margin*. Special Publication, vol. 5. Norwegian Petroleum Society, 167–198,
579 doi:10.1016/S0928-8937(06)80068-8, 1995.

580 Statoil, “Sleipner Øst, Volve Model, Hugin and Skagerrak Formation Petrophysical Evaluation, 2006”,
581 Stavanger, Norway. Accessed on: April, 27, 2019. Online: [https://www.equinor.com/volve-field-data-village-](https://www.equinor.com/volve-field-data-village-download)
582 [download](https://www.equinor.com/volve-field-data-village-download).

583 Strebelle, S., & Levy, M.: Using multiple-point statistics to build geologically realistic reservoir models: the
584 MPS/FDM workflow. Geological Society London, special publication, 309, 67-74, doi:10.1144/SP309.5, 2008.

585 Tetzlaff, D.M. & Harbaugh, J.W.: *Simulating Clastic Sedimentation*. New York: Van Nostrand Reinhold, 1989.

586 Varadi, M., Antonsen, P., Eien, M., & Hager, K.: Jurassic genetic sequence stratigraphy of the Norwegian block
587 15/5 area, South Viking Graben. In: Gradstein, F. M., Sandvik, K.O., & Milton, N.J., (eds) *Sequence Stratigraphy*
588 *– Concepts and Applications*. Norwegian Petroleum Society, Trondheim, special publication, 373-401, 1998.

589 Vollset, J. and Dore, A.G.: A revised Triassic and Jurassic lithostratigraphic nomenclature for the Norwegian North
590 Sea. *NPD Bulletin Oljedirektoratet*, 3, 53, 1984.

591 Walter C. P.: Relationship between eustacy and stratigraphic sequences of passive margins. *GSA Bulletin*; 89 (9),
592 1389–1403, 1978.

593 Winterer, L. W., Bosellini, A.: Subsidence and Sedimentation on Jurassic Passive Continental Margin, Southern
594 Alps, Italy. *AAPG Bulletin*; 65 (3), 394–421, doi: 10.1306/2F9197E2-16CE-11D7-8645000102C1865D, 1981.

595 Warrlich, G., Hillgartner, H., Rameil, N., Gittins, J., Mahruqi, I., Johnson, T., Alexander, D., Wassing, B.,
596 Steenwinkel, M., & Droste, H.: Reservoir characterisation of data-poor fields with regional analogues: a case study
597 from the Lower Shuaiba in the Sultanate of Oman, p. 577, 2010.

598 Zhong, D.: Transport Equation for Suspended Sediments Based on Two-Fluid Model of Solid/Liquid Two-Phase
599 Flows. *Journal of Hydraulic Engineering*; 137(5), 530-542, doi: 10.1061/(ASCE)HY.1943-7900.0000331, 2011.

List of Figures

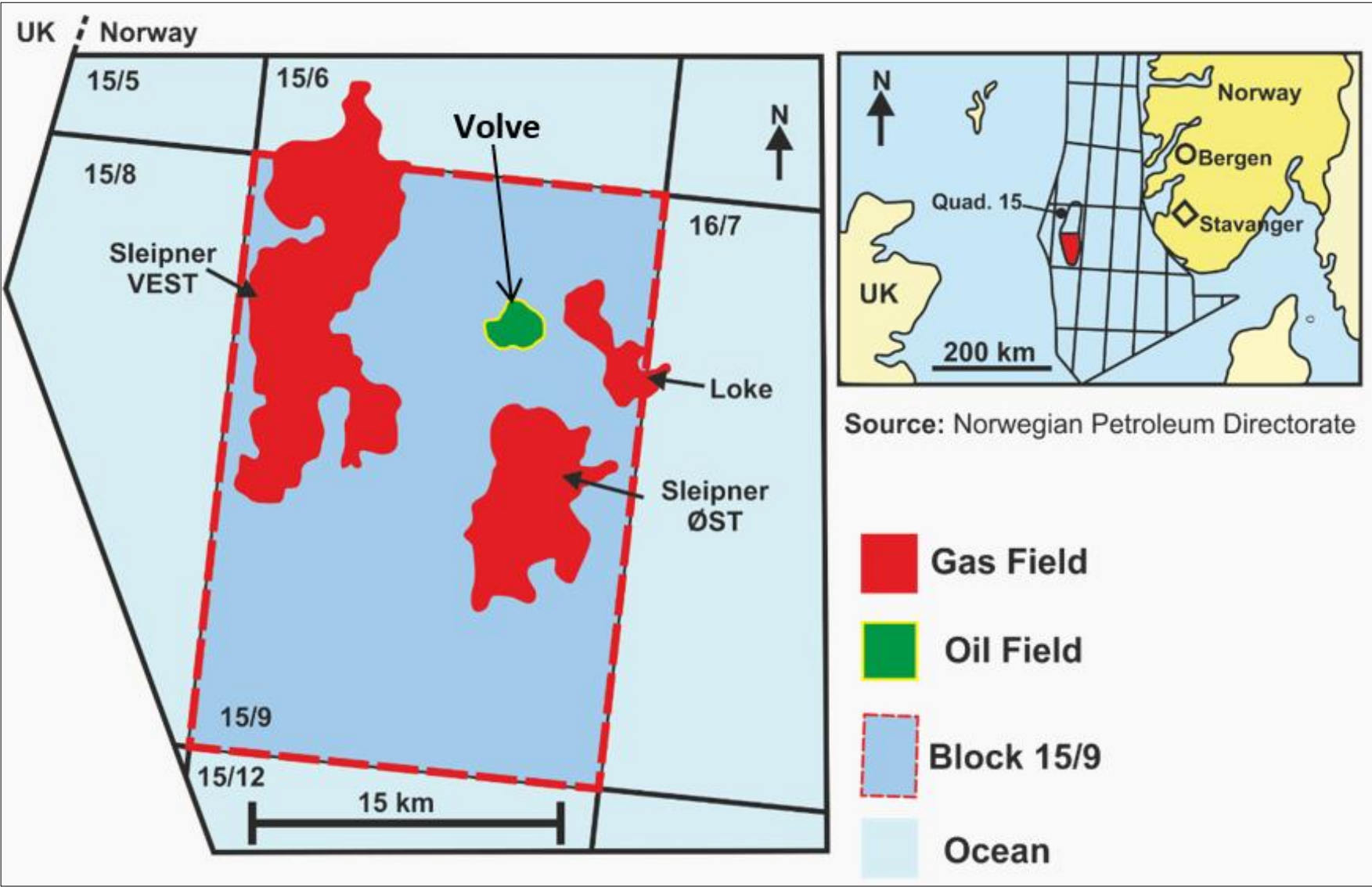


Fig 1. Location map of the Volve field; showing gas and oil fields in quadrant 15/9, Norwegian North Sea (from Ravasi et al., 2015).

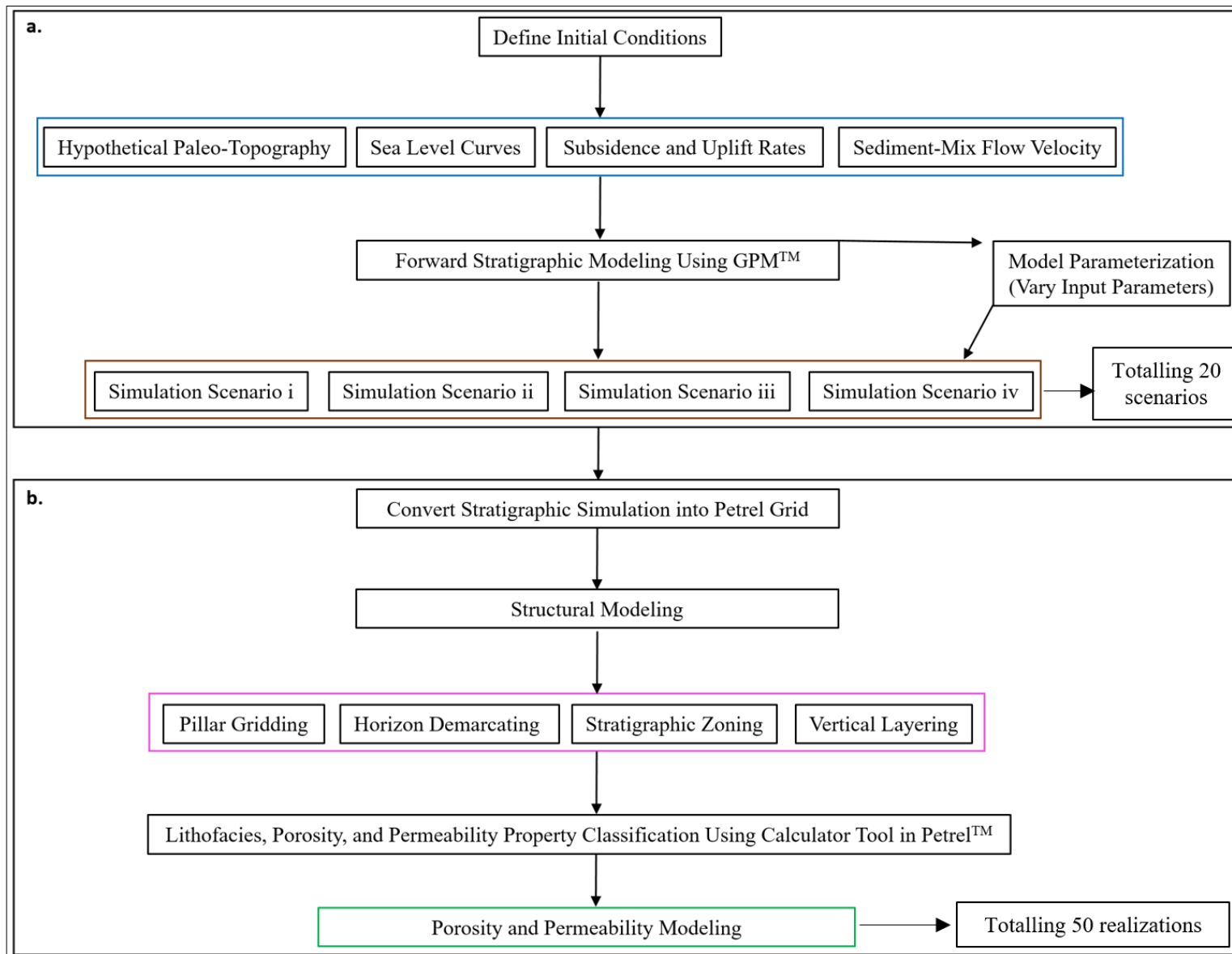


Fig 2. Schematic workflow of processes involved in this work. a. information of boundary conditions (input parameters) used for the forward stratigraphic simulation in GPM™; b. illustrate the use of forward stratigraphic models in Petrel™ for porosity and permeability modeling.

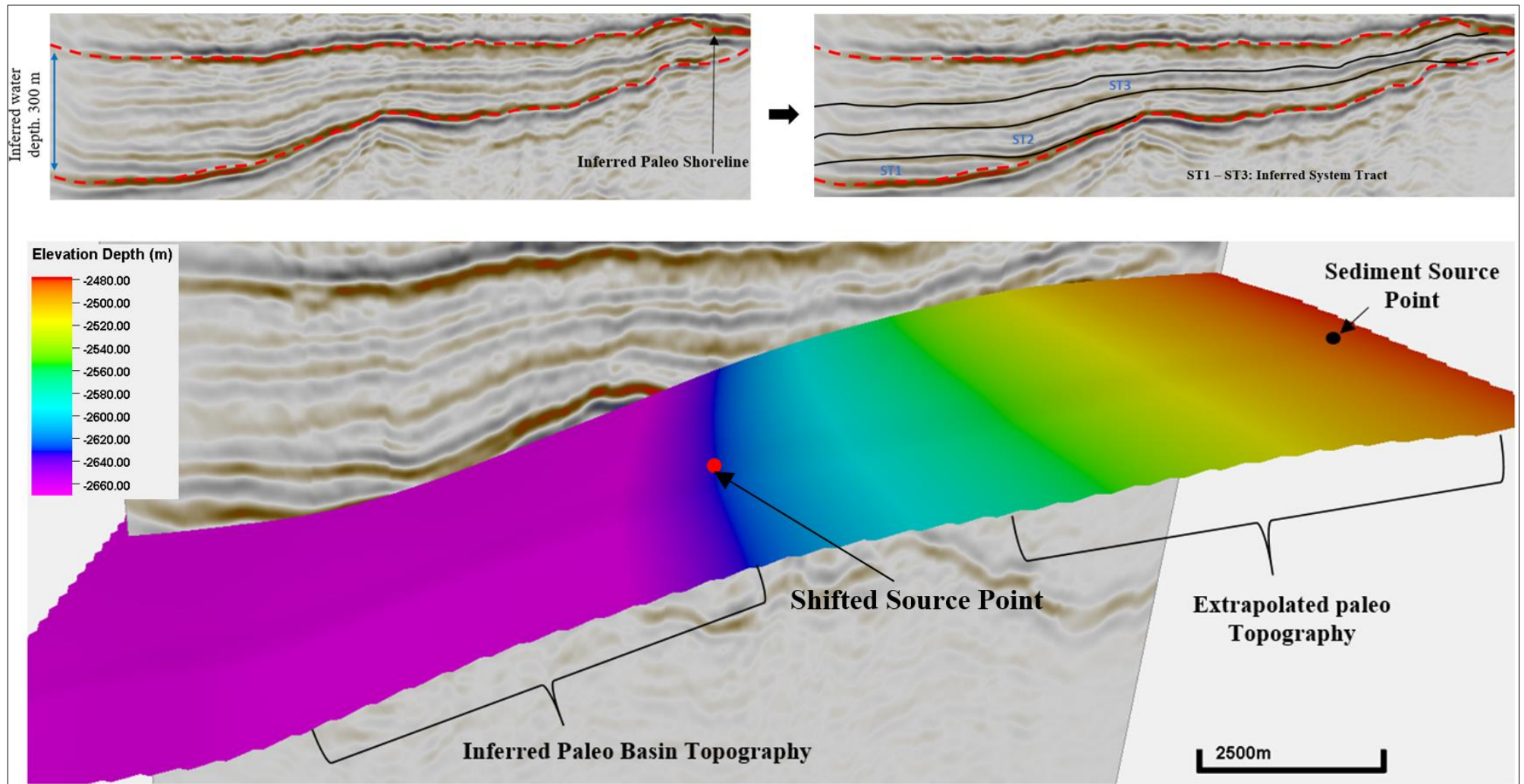


Fig 3. 3-D seismic section of the study area. Hypothetical topographic surface is derived from present-day base of reservoir. The sediment entry point into the basin is located in the North Eastern section (based on Kieft et al. 2011).

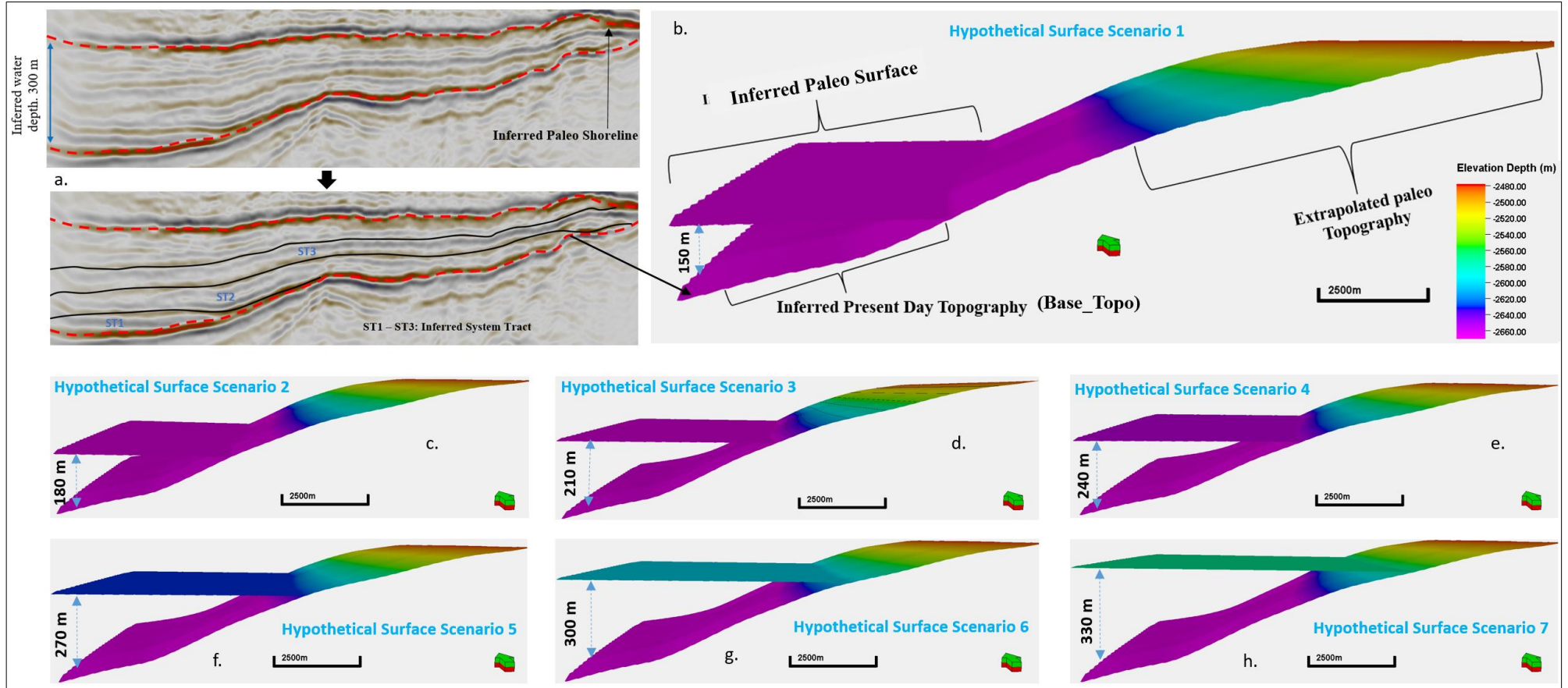


Fig 4. Illustrating a range of hypothetical initial topographic surfaces that were used to mitigate the uncertainty in selecting an initial topographic surface for the simulation. Considering that the topographic surface is a key control on stratigraphic sequence, different stratigraphic models are generated to attain a “best-fit” model.

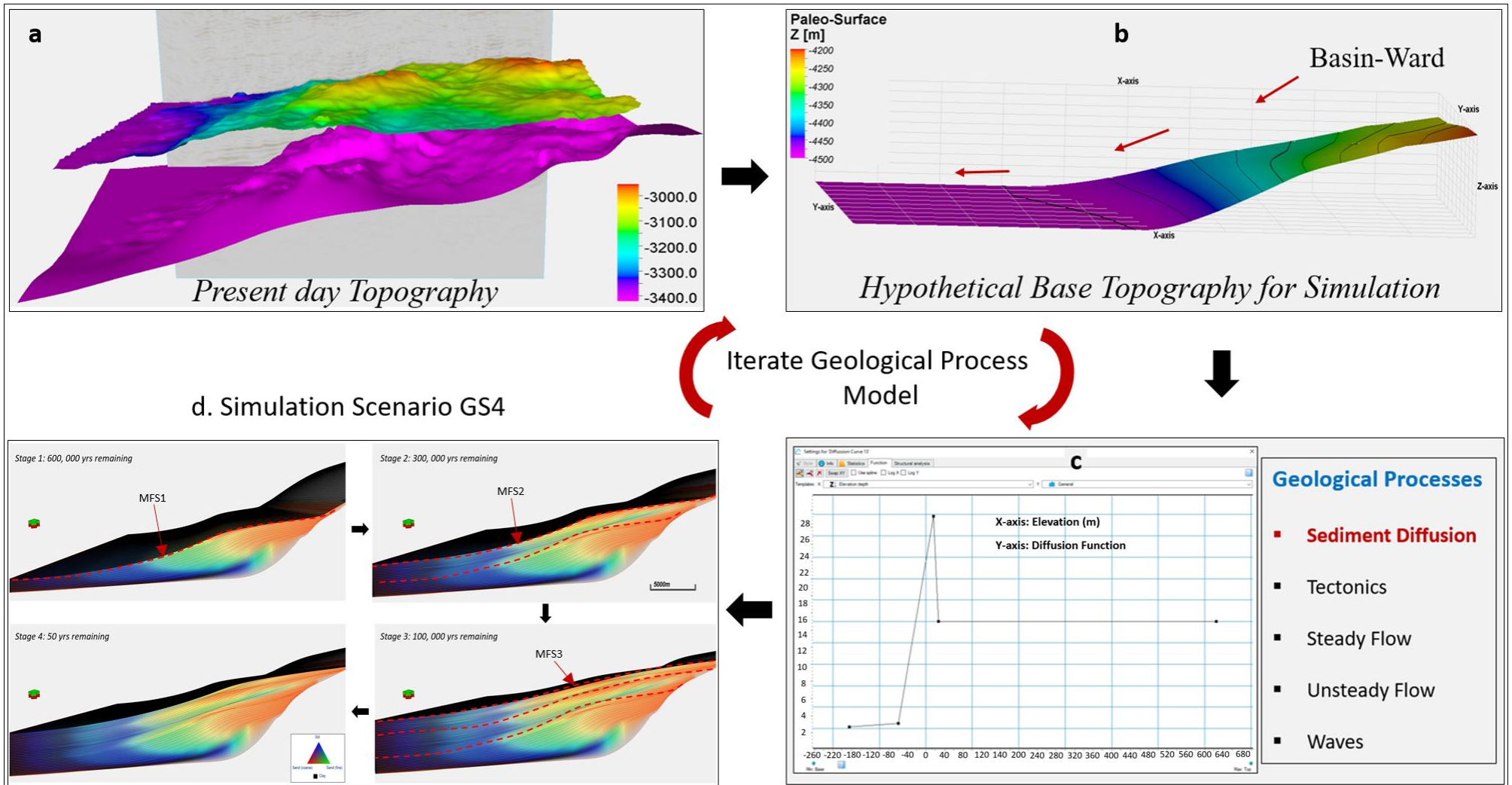


Fig 5. a. Present-day top and bottom topographic surfaces of the Hugin formation; b. hypothetical topographic surface after reprocessing of the base reservoir surface; c. stages of geological processes involved in the forward stratigraphic simulation; d. forward stratigraphic models at different time intervals of the simulation.

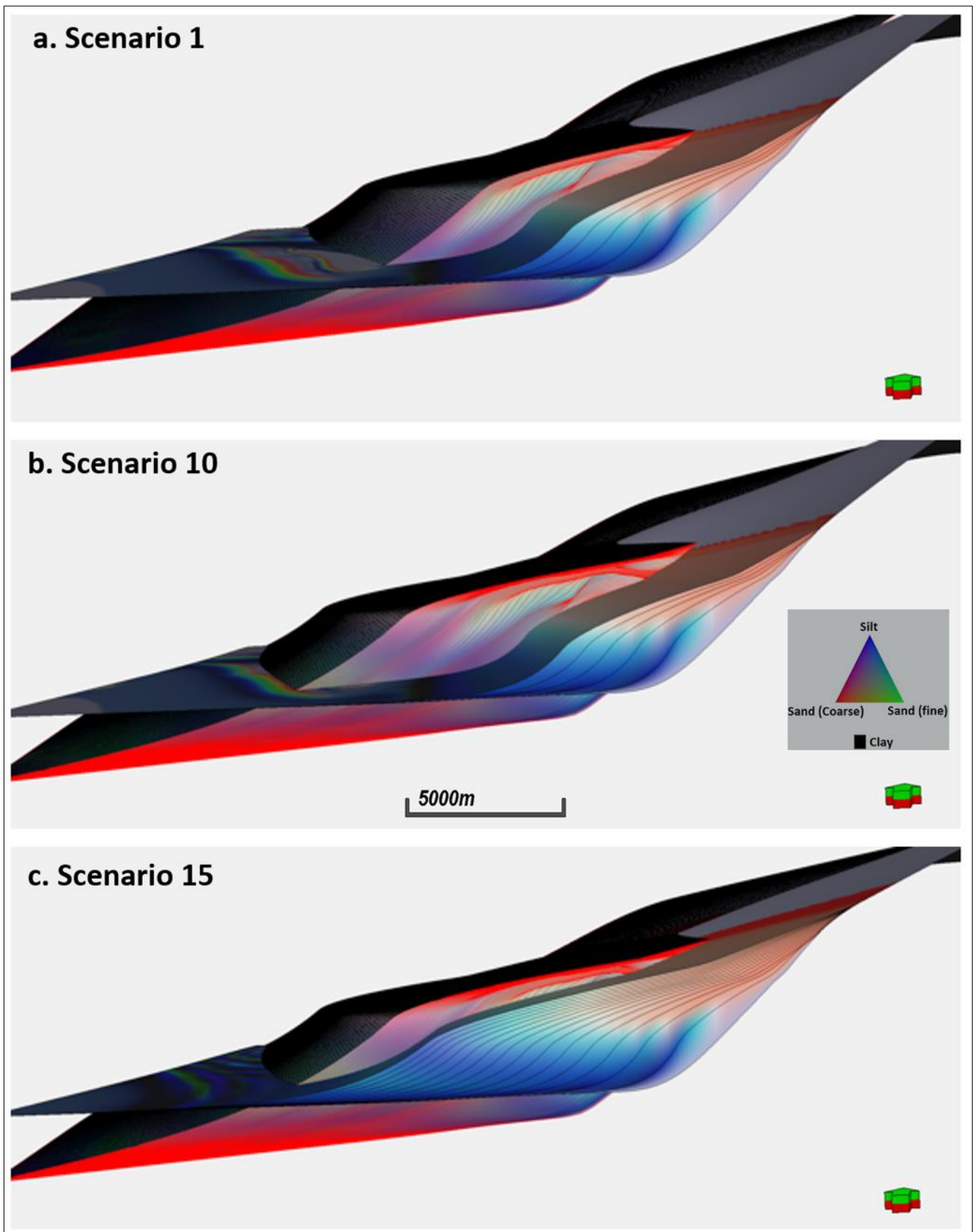


Fig 6. Example of stratigraphic simulation scenarios, from which the “best-fit” model was selected. **a.** involves the use of equal proportions of sediment supply, a relatively low subsidence rate and low water depth, **b.** applies a high proportions of fine sand and silt (70%) in the sediment mix, abrupt changes in subsidence rate, and a relatively high sea-level, **c.** involves very high proportions of fine sand and silt (80%), steady rate of subsidence and uplift in the sediment source area, and a relatively low water depth.

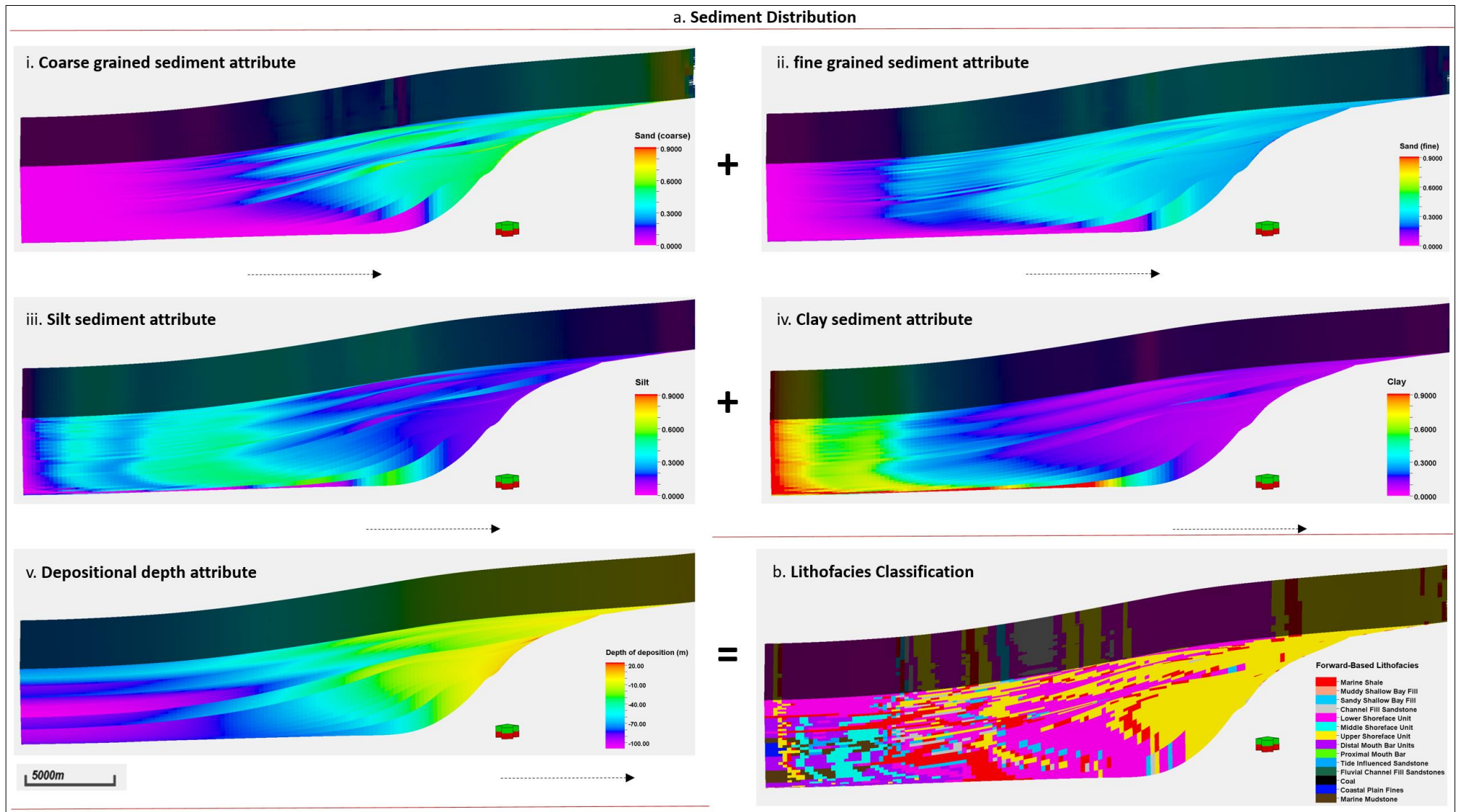


Fig 7 a. Sediment distribution patterns in the geological process modeling software. **b.** lithofacies classification using the property calculator tool in Petrel™.

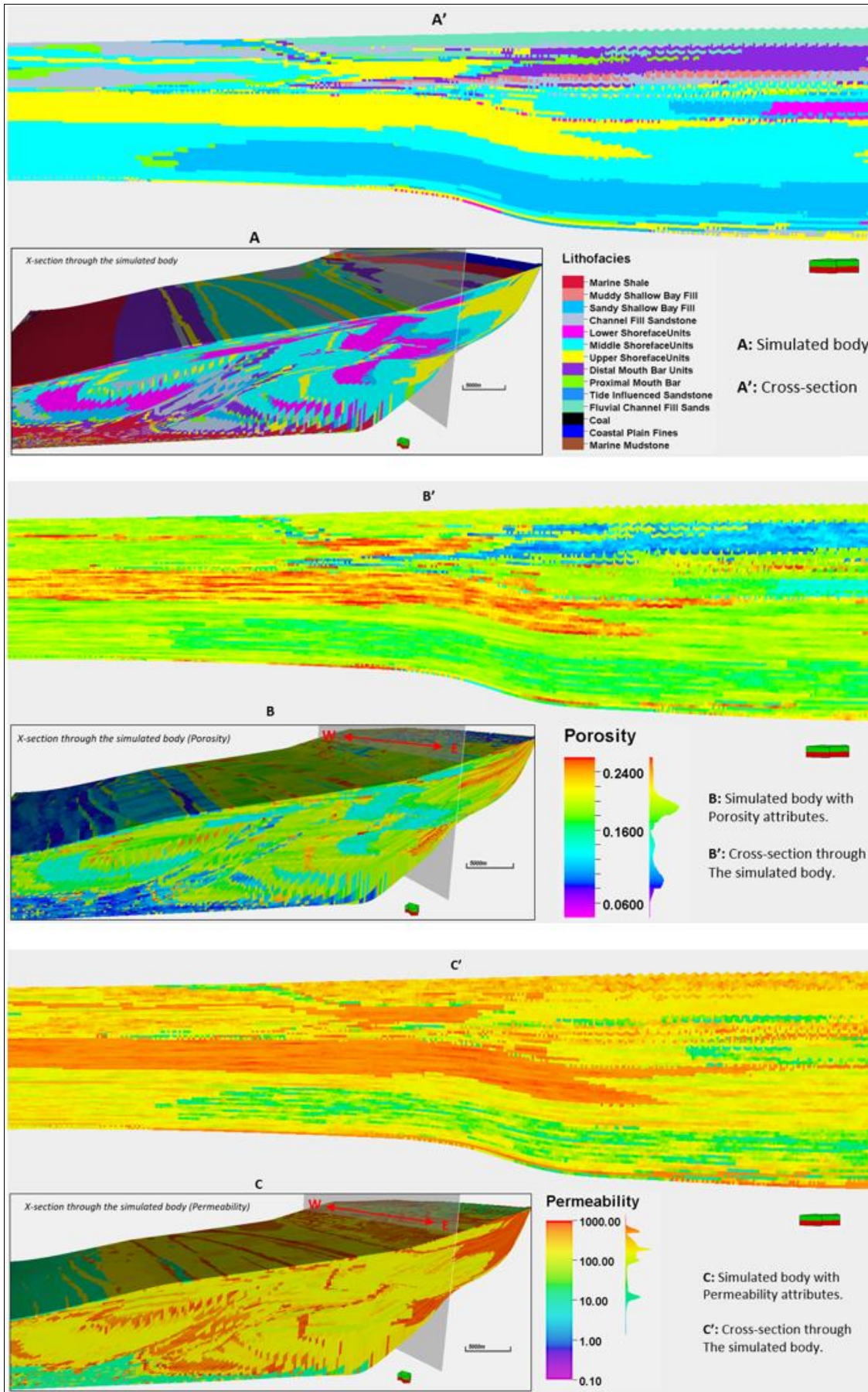


Fig 8. Lithofacies, porosity and permeability trends in the forward stratigraphic-based models.

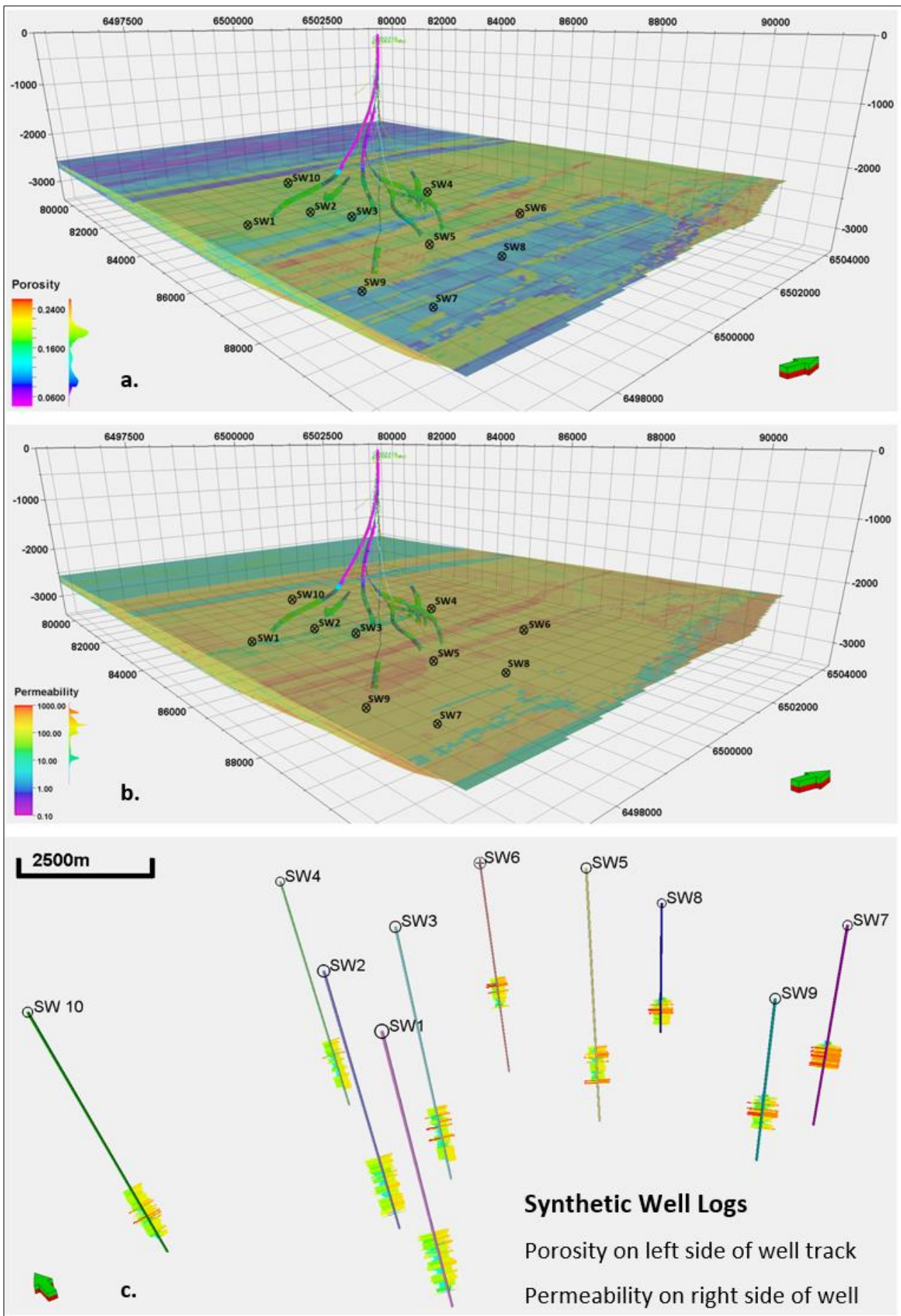


Fig 9. Synthetic wells forward stratigraphic-based porosity and permeability models. The average separation distance between wells is about 0.9 km.

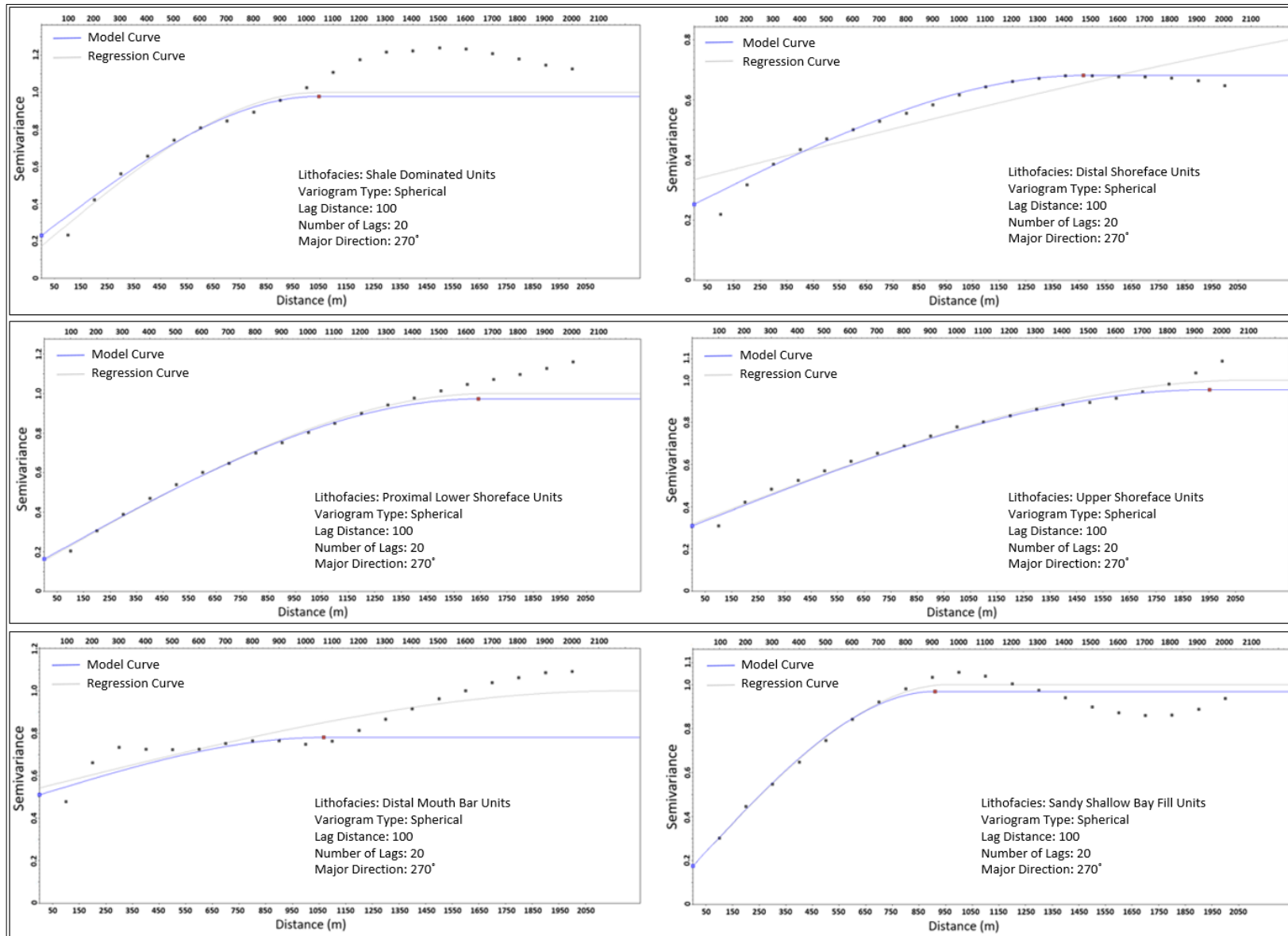


Fig 10. Variogram model of dominant lithofacies units from the forward stratigraphic model. The “dots” indicate the number of lags in the variogram through the major direction (NE-SW) of the stratigraphic model.

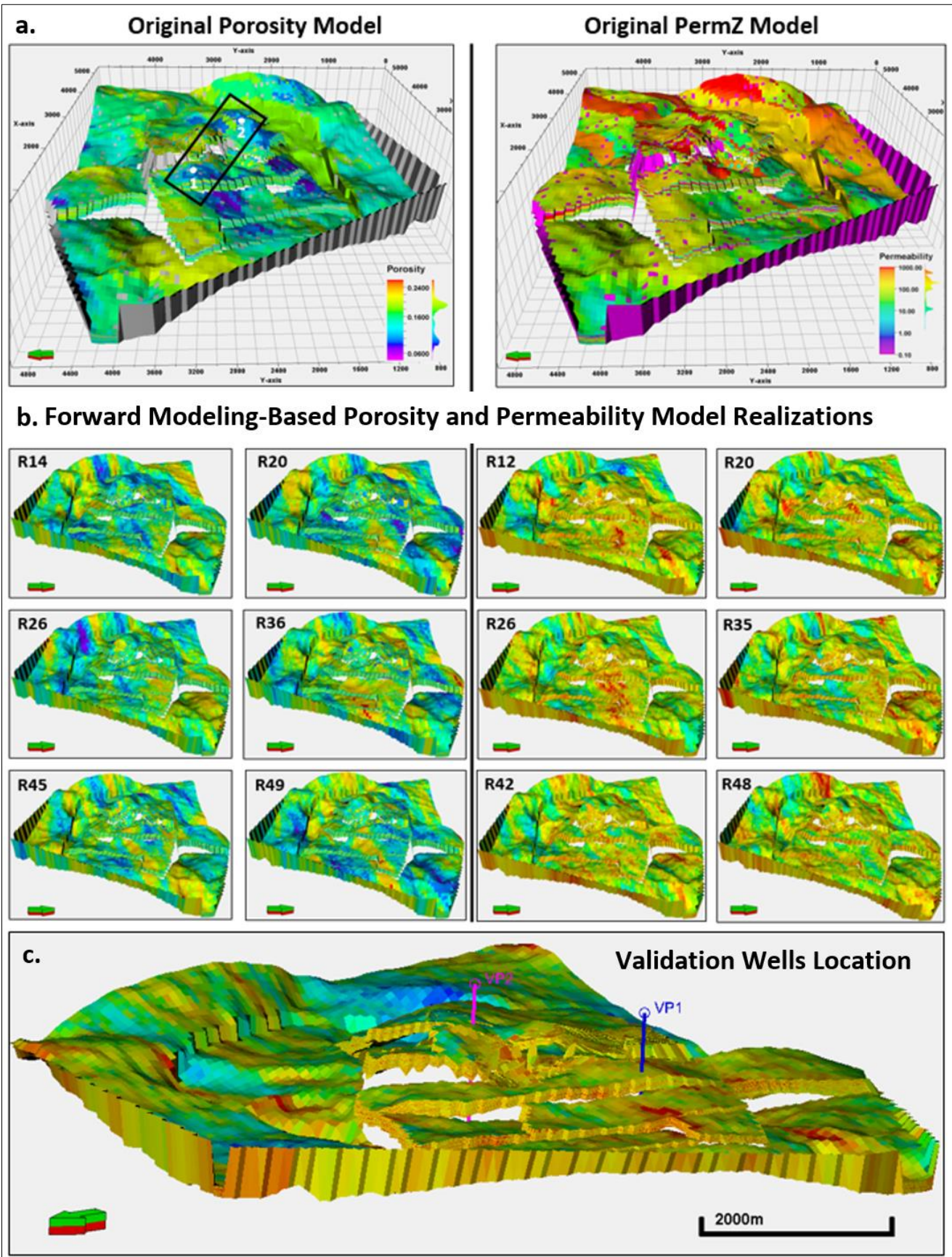


Fig 11. Comparing the Original Volve vs the forward modeling-based porosity and permeability models. Realizations 16, 20, 26, 36, 45, and 49 on the left half are porosity models, while realizations 12, 20, 26, 35, 42, and 48 on the right half are permeability models.

a. Validation Well 1

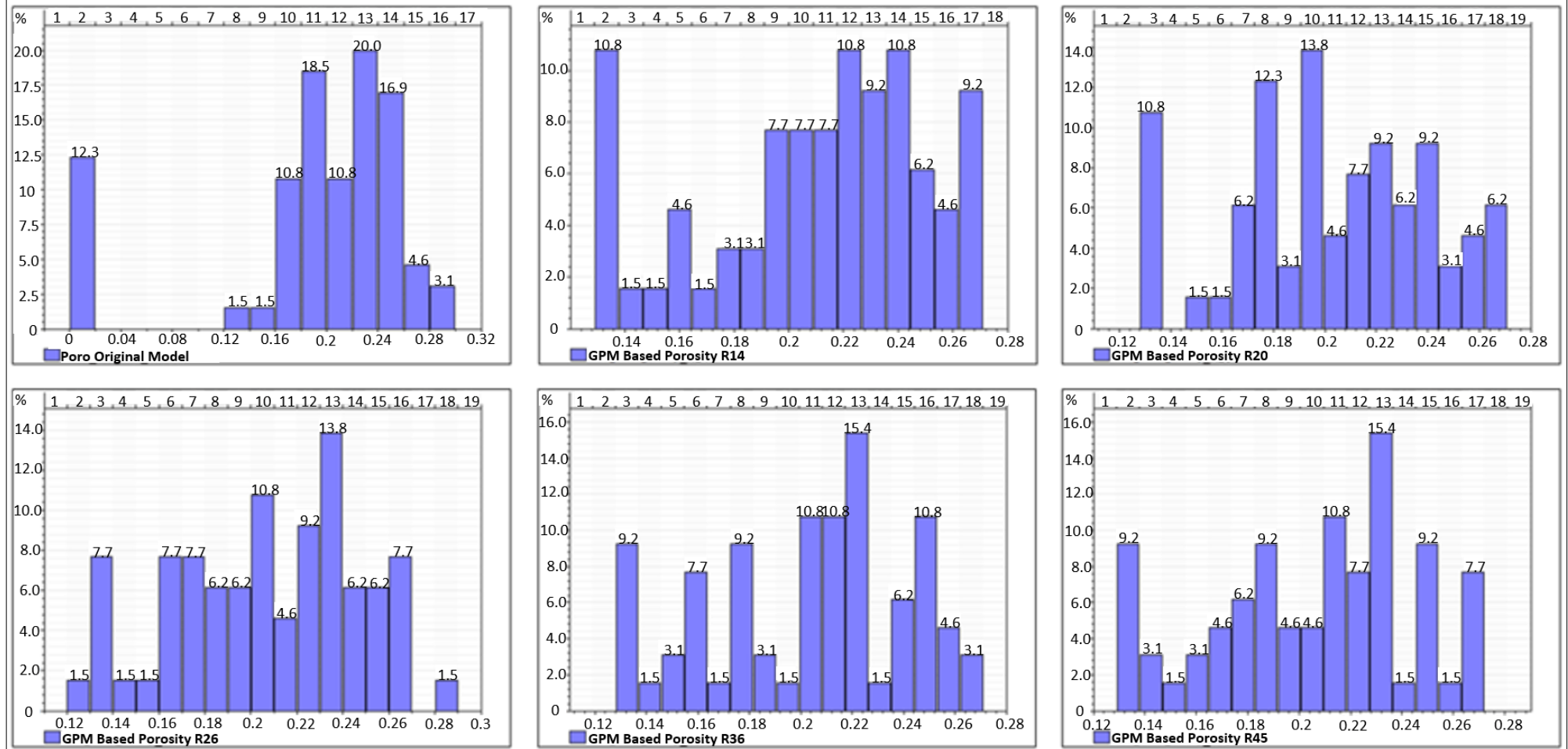


Fig 12a. Histogram illustrating porosity distribution in validation Well 1 of five stratigraphic-based realizations, and the original porosity model at identical vertical intervals.

b. Validation Well 2

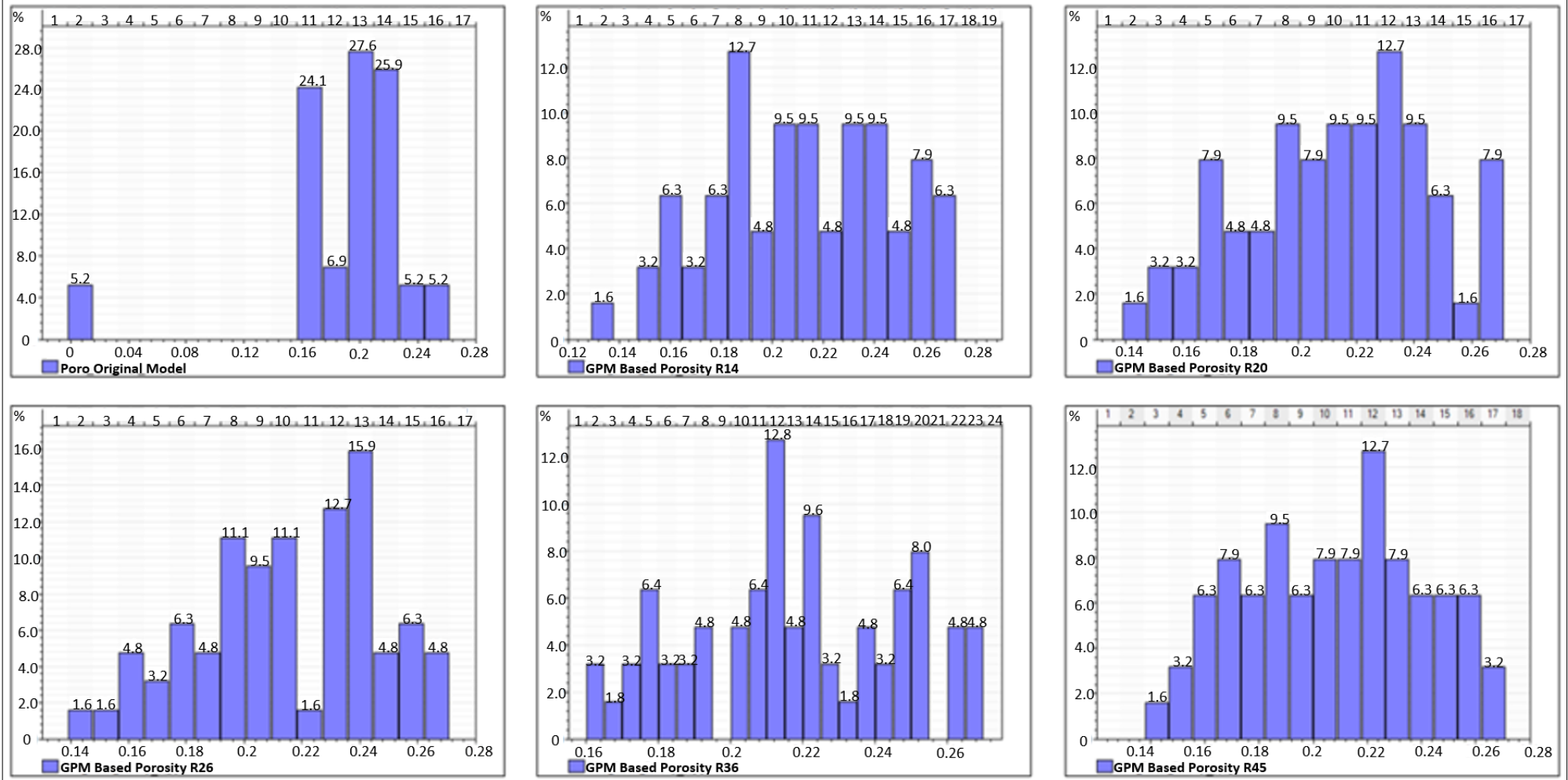


Fig 12b. Histogram illustrating porosity distribution in validation Well 2 of five stratigraphic-based realizations, and the original porosity model at identical vertical intervals.

Table 1 Lithofacies-associations in the Hugin formation, Volve Field (after Kieft et al. 2011).

| Code | Facies | Description | Thickness (t); Extent (l) | Wireline-log Attribute | Interpretation |
|----------|--------|---|---|--|---|
| A | A1 | Parallel-laminated mudstone with occasional siltstone inputs. Monospecific pattern of disorder bivalves parallel to bedding. | t = 30 - 425 cm l = 6 - 29 km | GR = 41 - 308 API DT = 225 - 355 μsm^{-1} NPHI = 0.17 - 0.45 v/v RHOB = 2280 - 2820 gcm^{-1} | Restricted marine shale |
| | A2 | Inter-bedded claystone and very fine-grained sandstone; non-parallel and wavy lamination. Scarcely bivalve shells oriented parallel to bedding. | t = 10 - 725 cm l = 8 - 13 km | GR = 17 - 65 API DT = 189 - 268 μsm^{-1} NPHI = ? RHOB = 2280 - 2820 gcm^{-1} | Muddy hallow bay fill |
| | A3 | Fine to medium grained sandstone; moderately to well sorted grain. Wavy bedding, cross bedding, rare wave ripples. | t = 60 - 370 cm l = 1 - 8 km | GR = 18 - 46 API DT = 199 - 268 μsm^{-1} NPHI = 0.07 - 0.52 v/v RHOB = 1690 - 2745 gcm^{-1} | Sandy shallow bay fill |
| | A4 | Parallel-laminated mudstone with occasional siltstone inputs. Monospecific pattern of disorder bivalves parallel to bedding. | t = 30 - 425 cm l = 6 - 29 km | GR = 7 - 35 API DT = 175 - 230 μsm^{-1} NPHI = 0.04 - 0.15 v/v RHOB = 2280 - 2820 gcm^{-1} | Marine channel fill sandstone |
| | B1 | Upward coarsening siltstone to fine-grained; moderatley sorted sandstone. Shell debris and quartz granules. | t = 30 - 480 cm l = 1 - 2 km | GR = 18 - 80 API DT = 168 - 291 μsm^{-1} NPHI = 0.04 - 0.191 v/v RHOB = 2322 - 2723 gcm^{-1} | Distal lower shoreface |
| B | B2 | Very fine-fine grained sandstone. Moderate to well sorted; fine grained carbonaceous laminae, typically low angle cross beds. | t = 130 - 440 cm l = 1.7 - 12 km | GR = 20 - 56 API DT = 179 - 277 μsm^{-1} NPHI = 0.05 - 0.168 v/v RHOB = 2314 - 2696 gcm^{-1} | Proximal lower shoreface |
| | B3 | Coaesening upward, cross laminated, fine to medium grained sandstone; consist of carbonaceous fragments. | t = 425 - 800 cm l = 1.7 - 8 km | GR = 15 - 25 API DT = 250 - 275 μsm^{-1} NPHI = 0.09 - 0.113 v/v RHOB = 2271 - 2342 gcm^{-1} | Upper shoreface |
| C | C1 | Highly bioturbated siltstone to very fine sandstone, with beds of rounded granules. | t = 175 - 1010 cm l = 7.2 - 19.6 km | GR = 20 - 80 API DT = 230 - 260 μsm^{-1} NPHI = 0.08 - 0.169 v/v RHOB = 2327 - 2521 gcm^{-1} | Distal mouth bar |
| | C2 | Very fine to fine grained sandstone, low angle cross bedding. | t = 290 - 775 cm l = 1 - 5 km | GR = 12 - 58 API DT = 167 - 397 μsm^{-1} NPHI = 0.05 - 0.595 v/v RHOB = 1612 - 2705 gcm^{-1} | Proximal mouth bar |
| D | D1 | Fining upward coarse to fine grained sandstone. Stacked fining upward beds with rare coarse grained stringers. | t = 740 - 820 cm l = 1 - 2 km | GR = 8 - 134 API DT = 235 - 335 μsm^{-1} NPHI = 0.14 - 0.46 v/v RHOB = 2284 - 2570 gcm^{-1} | Tidal influenced fluvial channel fill sandstone |
| | D2 | Fining upward coarse to medium grained sandstone. Carbonaceous laminae and fragments. Sharp and cohesive contact at base of bed. | t = 580 cm l = < 2 km | GR = 9 - 34 API DT = 241 - 297 μsm^{-1} NPHI = 0.14 - 0.289 v/v RHOB = 2168 - 2447 gcm^{-1} | fluvial channel fill sandstone |
| E | E1 | Coal and carbonaceous shale. Basal contact typically parallel, although maybe undulose. | t = 30 - 520 cm l = 6 - 19.6 km | GR = 8 - 56 API DT = 313 - 427 μsm^{-1} NPHI = 0.24 - 0.529 v/v RHOB = 1930 - 2225 gcm^{-1} | Coal |
| | E2 | Alternating dark grey mudstone/claystone and siltstone to very fine grained sandstone. Wavy to non-parallel lamination. | t = 60 cm l = < 2 km | GR = 32 - 60 API DT = 358 - 415 μsm^{-1} NPHI = 0.43 - 0.49 v/v RHOB = 1994 - 2148 gcm^{-1} | Coastal plain fines |
| F | F | Mudstone with rare siltstone beds. Parallel lamination, soft sediment deformation developed locally on top of beds. | t = section tot completely penetrated l = 1.7 - 36.7 km | GR = 4 - 134 API DT = 187 - 450 μsm^{-1} NPHI = 0.114 - 0.618 v/v RHOB = 1730 - 2925 gcm^{-1} | Open marine shale |

Table 2. Input parameters for forward stratigraphic simulations in GPM™

| | | Initial Conditions- GPM Input Parameters | | | | | | | | | | | | |
|---------------------------|----------------------|---|------------------------------|-------------------------------------|-----------------------------|-------------------------------------|---------------------|-------------------------------|--------------------|-----------------------|----------------|--------------------------|-----------------------|-------------------|
| | | Simulation Duration | Sediment Type Proportion (%) | | | | Avg. Water Velocity | Avg. Sediment Velocity | Erodibility | Diffusion Coefficient | Avg. Sea Level | Turbidite Event Interval | Steady Flow Iteration | Sediment Movement |
| | | | (Ma- 0a) Years | Sand (Coarse) | Sand (Fine) | Silt | Clay | (m/a) | | | (m/a) | Interval (m) | (/years) | (/hrs) |
| GPM Scenarios (GS) | S1 | 0.02 – 0 | 25 | 25 | 25 | 25 | 0.11 | 0.03 | 0.35 | 0.11 | 30 | 2500 | 10 | 0.001 |
| | S2 | 0.25 – 0 | 25 | 25 | 25 | 25 | 0.15 | 0.03 | 0.45 | 0.15 | 70 | 1000 | 15 | 0.012 |
| | S3 | 0.5 – 0 | 25 | 25 | 25 | 25 | 0.11 | 0.02 | 0.55 | 0.11 | 120 | 1000 | 20 | 0.012 |
| | S4 | 0.7 – 0.05 | 25 | 25 | 25 | 25 | 0.08 | 0.02 | 0.35 | 0.08 | 100 | 500 | 25 | 0.0011 |
| | S5 | 1.5 – 0 | 15 | 35 | 30 | 20 | 0.15 | 0.04 | 0.50 | 0.15 | 80 | 5000 | 20 | 0.001 |
| | S6 | 3.0 – 0 | 50 | 25 | 15 | 10 | 0.13 | 0.04 | 0.50 | 0.13 | 70 | 5000 | 30 | 0.0012 |
| | S7 | 3.5 – 0 | 50 | 25 | 15 | 10 | 0.11 | 0.04 | 0.50 | 0.11 | 70 | 10000 | 15 | 0.001 |
| | S8 | 4.0 – 0 | 50 | 25 | 15 | 10 | 0.13 | 0.04 | 0.50 | 0.13 | 90 | 5000 | 20 | 0.0015 |
| | S9 | 4.5 – 0 | 15 | 45 | 25 | 15 | 0.1 | 0.02 | 0.45 | 0.1 | 50 | 10000 | 30 | 0.0012 |
| | S10 | 5.0 – 0 | 15 | 45 | 25 | 15 | 0.12 | 0.02 | 0.45 | 0.12 | 55 | 10000 | 35 | 0.0013 |
| | S11 | 5.5 - 0 | 15 | 45 | 25 | 15 | 0.12 | 0.02 | 0.45 | 0.12 | 40 | 5000 | 40 | 0.0013 |
| | S12 | 6.0 – 0 | 15 | 45 | 25 | 15 | 0.1 | 0.02 | 0.45 | 0.1 | 60 | 10000 | 35 | 0.0011 |
| | S13 | 6.5 – 0 | 10 | 25 | 55 | 10 | 0.13 | 0.03 | 0.48 | 0.13 | 100 | 20000 | 50 | 0.0010 |
| | S14 | 7.0 – 0 | 10 | 25 | 55 | 10 | 0.16 | 0.03 | 0.48 | 0.16 | 40 | 20000 | 45 | 0.0011 |
| | S15 | 7.5 – 0 | 10 | 25 | 55 | 10 | 0.13 | 0.03 | 0.48 | 0.13 | 40 | 20000 | 40 | 0.0012 |
| | S16 | 8.0 – 0 | 10 | 25 | 55 | 10 | 0.15 | 0.03 | 0.48 | 0.15 | 30 | 10000 | 30 | 0.0010 |
| | S17 | 8.5 – 0 | 10 | 25 | 45 | 20 | 0.14 | 0.02 | 0.45 | 0.14 | 50 | 50000 | 50 | 0.0010 |
| | S18 | 9.0 – 0 | 30 | 30 | 18 | 22 | 0.13 | 0.02 | 0.52 | 0.13 | 60 | 25000 | 35 | 0.0012 |
| | S19 | 9.5 – 0 | 30 | 40 | 12 | 18 | 0.12 | 0.02 | 0.55 | 0.12 | 55 | 25000 | 20 | 0.0013 |
| | S20 | 10.0 - 0 | 30 | 42 | 18 | 10 | 0.11 | 0.01 | 0.40 | 0.11 | 50 | 5000 | 15 | 0.0011 |
| Sediment Property | | | | | | | | | | | | | | |
| | Sediment Type | Diameter | Density | Initial Porosity | Initial Permeability | Compacted Porosity | Compaction | Compacted Permeability | Erodibility | | | | | |
| | Coarse Grained Sand | 1.0 mm | 2.70 g/cm ³ | 0.21 m ³ /m ³ | 500 mD | 0.25 m ³ /m ³ | 5000 KPa | 50 mD | 0.6 | | | | | |
| | Fine Grained Sand | 0.1 mm | 2.70 g/cm ³ | 0.3 m ³ /m ³ | 100 mD | 0.15 m ³ /m ³ | 2500 KPa | 5 mD | 0.45 | | | | | |
| | Silt | 0.01 mm | 2.65 g/cm ³ | 0.38 m ³ /m ³ | 50 mD | 0.12 m ³ /m ³ | 1200 KPa | 2 mD | 0.3 | | | | | |
| | Clay | 0.001 mm | 2.65 g/cm ³ | 0.48 m ³ /m ³ | 5 mD | 0.05 m ³ /m ³ | 500 KPa | 0.1 mD | 0.15 | | | | | |

Table 3. Lithofacies classification in the forward stratigraphic model by using the property calculator tool in Petrel™.

| Lithofacies Classification | | |
|----------------------------|----------------------------|--|
| Facies Code | Lithofacies | Command Used in Petrel's Property Calculator |
| 0 | Marine Shale | If(Sand_fine>=0.19 And Sand_fine<=0.21 Or Silt>=0.19 And Silt<=0.2 Or Clay>=0.2 And Clay<=0.21 Or Depth_of_deposition>=-82 And Depth_of_deposition<=-78) |
| 1 | Muddy Shallow Bay Fill | If(Sand_fine>=0.36 And Sand_fine<=0.38 Or Silt>=0.18 And Silt<=0.2 Or Clay>0.18 And Clay<=0.19 Or Depth_of_deposition>=-30 And Depth_of_deposition<=-20) |
| 2 | Sandy Shallow Bay Fill | If(Sand_coarse>=0.65 And Sand_coarse<=0.73 Or Sand_fine>=0.18 And Sand_fine<=0.22 Or Silt>=0.18 And Silt<=0.2 Or Clay>=0.17 And Clay<=0.18 Or Depth_of_deposition>=-3 And Depth_of_deposition<=0) |
| 3 | Channel Fill Sandstone | If(Sand_coarse>=0.5 And Sand_coarse<=0.68 Or Sand_fine>=0.23 And Sand_fine<=0.25 Or Silt>=0.17 And Silt<=0.18 Or Depth_of_deposition>=0 And Depth_of_deposition<=2) |
| 4 | Lower Shoreface Units | If(Sand_coarse>=0.19 And Sand_coarse<=0.31 Or Sand_fine>=0.19 And Sand_fine<=0.24 Or Silt>=0.4 And Silt<=0.48 Or Clay>=0.19 And Clay<=0.31 Or Depth_of_deposition>=-83 And Depth_of_deposition<=50) |
| 5 | Middle Shoreface Units | If(Sand_coarse>=0.32 And Sand_coarse<=0.53 Or Sand_fine>=0.25 And Sand_fine<=0.32 Or Silt>=0.26 And Silt<=0.32 Or Clay>=0.19 And Clay<=0.21 Or Depth_of_deposition>=-38 And Depth_of_deposition<=-12) |
| 6 | Upper Shoreface Units | If(Sand_coarse>=0.53 And Sand_coarse<=0.72 Or Sand_fine>=0.28 And Sand_fine<=0.33 Or Silt>=0.16 And Silt<=0.21 Or Depth_of_deposition>=-10 And Depth_of_deposition<=6) |
| 7 | Distal Mouth Bar Units | If(Sand_fine>=0.23 And Sand_fine<=0.27 Or Silt>=0.38 And Silt<=0.43 Or Clay>=0.19 And Clay<=0.21 Or Depth_of_deposition>=-95 And Depth_of_deposition<=-80) |
| 8 | Proximal Mouth Bar Units | If(Sand_coarse>=0.53 And Sand_coarse<=0.71 Or Sand_fine>=0.27 And Sand_fine<=0.32 Or Silt>=0.16 And Silt<=0.21 Or Clay>=0.06 And Clay<=0.07 Or Depth_of_deposition>=-30 And Depth_of_deposition<=-27) |
| 9 | Tide Influenced Sandstones | If(Sand_coarse>=0.53 And Sand_coarse<=0.71 Or Sand_fine>=0.26 And Sand_fine<=0.31 Or Silt>=0.35 And Silt<=0.41 Or Depth_of_deposition>=-5 And Depth_of_deposition<=1) |
| 10 | Fluvial Channel Sandstones | If(Sand_coarse>=0.54 And Sand_coarse<=0.56 Or Sand_fine>=0.27 And Sand_fine<=0.29 Or Silt>=0.19 And Silt<=0.21 Or Depth_of_deposition>=-2 And Depth_of_deposition<=2) |
| 11 | Coal | Estimated as background attribute |
| 12 | Coastal plain fines | If(Silt>=0.31 And Silt<=0.43 Or Clay>=0.31 And Clay<=0.35 Or Depositional_depth>=-100 And Depositional_depth<=-40) |
| 13 | Marine Mudstone | If(Sand_fine>=0.36 And Sand_fine<=0.38 Or Silt>=0.4 And Silt<=0.52 Or Clay>=0.45 And Clay<=0.78 Or Depth_of_deposition>=-105 And Depth_of_deposition<=-90) |

Table 4. Porosity and Permeability estimates of lithofacies packages in the model area.

| Code | Lithofacies | Avg. NPHI | Density Porosity | Estimated Porosity | KLOGH (mD) |
|-------------|----------------------------|------------------|-------------------------|---------------------------|-------------------|
| 0 | Marine Shale | 0.17 - 0.45 | 0.1 | 0.08 - 0.11 | 10.02 - 16.1 |
| 1 | Muddy Shallow Bay Fill | 0.17 - 0.42 | 0.1 | 0.08 - 0.13 | 23.85 - 102.3 |
| 2 | Sandy Shallow Bay Fill | 0.07 - 0.52 | 0.25 | 0.16 - 0.25 | 100.0 - 398.7 |
| 3 | Channel Fill Sandstone | 0.04 - 0.15 | 0.3 | 0.18 - 0.22 | 400.01 - 889.7 |
| 4 | Distal Lower Shoreface | 0.04 - 0.19 | 0.29 | 0.1 - 0.23 | 120.5 - 170.3 |
| 5 | Proximal Shoreface | 0.05 - 0.17 | 0.31 | 0.17 - 0.24 | 80.2 - 412.5 |
| 6 | Upper Shoreface | 0.09 - 0.11 | 0.28 | 0.21 - 0.26 | 650.2 - 1023.7 |
| 7 | Distal Mouth Bar | 0.08 - 0.17 | 0.27 | 0.09 - 0.17 | 170.5 - 223.1 |
| 8 | Proximal Mouth Bar | 0.05 - 0.59 | 0.12 | 0.19 - 0.21 | 130.5 - 314.3 |
| 9 | Tidal Influenced Sandstone | 0.14 - 0.46 | 0.26 | 0.15 - 0.20 | 220.0 - 512.6 |
| 10 | Fluvial Sandstones | 0.14 - 0.29 | 0.21 | 0.19 - 0.21 | 180.5 - 691.8 |
| 11 | Coal | 0.24 - 0.53 | 0.05 | 0.001 | 0.001 |
| 12 | Coastal Plain Fines | 0.43 - 0.49 | 0.06 | 0.04 - 0.12 | 5.2 - 34.6 |
| 13 | Marine Mudstone | 0.16 - 0.42 | 0.1 | 0.08 - 0.10 | 6.0 - 15.2 |

Table 5. A comparison of a) porosity, and b) permeability estimates from selected intervals in the original porosity/permeability models and forward modeling-based porosity and permeability models.

| a. Validation Well Position 1 | | | | | |
|--------------------------------------|-------------------------------------|--------|--------|--------|--------|
| | Depth (m) | | | | |
| | 5 m | 10 m | 15 m | 25 m | 35 m |
| Models | Measured Porosity | | | | |
| Original Model | 0.2 | 0.25 | 0.27 | 0.16 | 0.13 |
| R14 | 0.22 | 0.24 | 0.16 | 0.22 | 0.16 |
| R20 | 0.16 | 0.19 | 0.26 | 0.18 | 0.15 |
| R26 | 0.18 | 0.17 | 0.23 | 0.16 | 0.19 |
| R36 | 0.22 | 0.21 | 0.19 | 0.22 | 0.21 |
| R45 | 0.25 | 0.2 | 0.23 | 0.22 | 0.15 |
| R49 | 0.21 | 0.17 | 0.22 | 0.17 | 0.18 |
| Validation Well Position 2 | | | | | |
| | Depth (m) | | | | |
| | 5 m | 10 m | 15 m | 25 m | 35 m |
| Models | Measured Porosity | | | | |
| Original Model | 0.17 | 0.21 | 0.21 | 0.17 | 0.19 |
| R14 | 0.17 | 0.16 | 0.24 | 0.15 | 0.25 |
| R20 | 0.21 | 0.22 | 0.2 | 0.21 | 0.23 |
| R26 | 0.21 | 0.2 | 0.21 | 0.25 | 0.24 |
| R36 | 0.2 | 0.22 | 0.21 | 0.21 | 0.19 |
| R45 | 0.22 | 0.19 | 0.2 | 0.19 | 0.21 |
| R49 | 0.26 | 0.24 | 0.23 | 0.16 | 0.21 |
| b. Validation Well Position 1 | | | | | |
| | Depth (m) | | | | |
| | 5 m | 10 m | 15 m | 25 m | 35 m |
| Models | Measured Permeability_Z (mD) | | | | |
| Original Model | 352.74 | 312.38 | 201.08 | 199.76 | 508.2 |
| R14 | 163.95 | 312.38 | 69.84 | 310.16 | 508.2 |
| R20 | 290.84 | 315.09 | 105.66 | 273.04 | 200.63 |
| R26 | 375.92 | 203.81 | 166.23 | 189.92 | 348.12 |
| R36 | 418.03 | 203.27 | 190.9 | 168.9 | 370.56 |
| R45 | 337.6 | 412.67 | 199.66 | 156.71 | 305.92 |
| R49 | 370.89 | 129.33 | 291.77 | 175.53 | 551.18 |
| Validation Well Position 2 | | | | | |
| | Depth (m) | | | | |
| | 5 m | 10 m | 15 m | 25 m | 35 m |
| Models | Measured Permeability_Z (mD) | | | | |
| Original Model | 6.6 | 883.6 | 30.3 | 496.99 | 156.6 |
| R14 | 320.34 | 336.22 | 151.08 | 464.22 | 132.98 |
| R20 | 122.66 | 209.15 | 161.3 | 230.58 | 208.48 |
| R26 | 151.48 | 710.07 | 175.09 | 384.49 | 169.48 |
| R36 | 184.74 | 344.99 | 157.08 | 420.15 | 136.14 |
| R45 | 91.44 | 361.04 | 77.17 | 382.85 | 134.56 |
| R49 | 134.01 | 721.73 | 137.42 | 636.48 | 290.06 |